Electronic Supporting Information (ESI):

Template-free synthesis of mesoporous, amorphous transition metal phosphate materials

Stephanos Karafiludis[1,2*], Ana Guilherme Buzanich[1], Christian Heinekamp[1,2], Annett Zimathies[1], Glen J. Smales[1], Vasile-Dan Hodoroaba[1], Johan E. ten Elshof[3], Franziska Emmerling[1,2] and Tomasz M. Stawski[1**]

[1]Federal Institute for Materials Research and Testing, Unter den Eichen 87, 12205 Berlin, Germany

[2]Department of Chemistry, Humboldt-Universität zu Berlin, Brook-Taylor-Straße 2, 12489 Berlin, Germany

[3]MESA+ Institute for Nanotechnology, University of Twente, P.O. Box 217, 7500 AE Enschede, the Netherlands

Stephanos Karafiludis: https://orcid.org/0000-0002-7257-6311;
Ana Guilherme Buzanich: https://orcid.org/0000-0001-5543-9924;
Christian Heinekamp: https://orcid.org/0000-0003-4306-2909 ;
Glen J. Smales: https://orcid.org/0000-0002-8654-9867 ;
Vasile-Dan Hodoroaba: https://orcid.org/0000-0002-7901-6114 ;
Johan E. Ten Elshof: https://orcid.org/0000-0001-7995-6571 ;
Franziska Emmerling: https://orcid.org/0000-0001-8528-0301;
Tomasz M. Stawski: https://orcid.org/0000-0002-0881-5808;

Keywords: transition metals, phosphate, struvite, mesoporosity, amorphous phases, thermal treatment, scattering, X-ray absorption spectroscopy

Corresponding authors: **tomasz.stawski@bam.de ;* stephanos.karafiludis@bam.de

Table of Contents

List of Figures

List of Equations

List of Tables

Supplementary Note 1: Critical analysis of SAXS and WAXS processing and of the applied fitting model

The SAXS and WAXS data were measured simultaneously by two different detectors, a Dectris Pilatus 1M for SAXS, and at wide angles with Dectris Pilatus 300k. In principle for our configuration, where the SAXS detector was placed at 1.2 m from the sample, the signal from SAXS and WAXS should overlap in the narrow q-range between 5.76 and 7.36 nm^{-1}. In such a way merging SAXS and WAXS is possible by scaling the WAXS intensity against SAXS. The SAXS signal is normalized against the readout from the photo diode and the primary beam monitor, while WAXS is not. Likewise, the background correction in WAXS should be performed based on the transmission factors from SAXS. However, in practice such scaling was for some samples (e.g. Mg-struvite) quite challenging. The issues could be caused by the fact that both detectors had different shapes and resolutions, and the measured signal was distorted at the edges of the detectors differently. Despite applying correction algorithms, the relatively confined overlap q-range led to high uncertainties, especially for the samples with low signal-to-background ratio. Therefore, we analyzed/fitted the SAXS data in detail and used the WAXS signal only for phase identification and transitions. The merging of SAXS/WAXS would present all raw data in one diffraction curve, but with no additional information gain, because the WAXS region represents a molecular structure of the samples, which is not considered in the scattering model in the first place. Due to the difficulties mentioned, in some samples, we kept the WAXS normalized against the SAXS data but separated the diffraction signals to avoid a misleading data visualization.

A hard-sphere model was used for all SAXS fits. Our general assumption is that the initial pore geometry is approximated by an isotropic, near spherical-like structure forming due to degassing of ammonia and water. The model considers hard-(sphere) potential-type particle/pore interactions which is more realistic in these systems hinted by the occurrence of broad correlation peaks in the SAXS data.

As the developing meso- and microporous signal in the M-struvite components changes significantly in time in the q position and intensity, a significant interference of the pores is assumed to occur in agreement with other SAXS studies of phosphate materials [1-3]. As we observed these hard-sphere interactions, this model reflects quite accurately the real pore structure of the sample as it considers interparticle/interpore interference [4, 5]. These interpore interactions demonstrate themselves as broad maxima/pseudo-peaks in the scattering pattern. In the model (Equation S1) one of the independent parameters, the fixed local volume fraction ν, influences the intensity and the width of such local maxima. The radius size distribution of the pores, composed of many hard sphere radii R_{Hs}, impacts their position in q. In our data evaluation method, ν cannot be fitted as a parameter, but instead it has to be kept constant. In turn for a given fixed ν, we obtained the size distributions of R_{HS}. Depending on the convergence of the fit, ranges of local volume fractions, typically between $35\% \leq \nu \leq 50\%$ were explored as input values to obtain a significant fit (SI: Figure S11 and Figure S12). Within this window, a ν = 40% was optimal to fit micro- and mesoporosity simultaneously occurring in the samples (SI: Figure S15-S17). Based on the BJH cumulative pore volume from BET and the known bulk densities of the different M-struvite powders, a similar value for the pore volume fraction was obtained for our results (SI: Equation S1) and results in the literature [1]. This indicates that the ν approximated from the convergence of the fits and the determined ν from BET agree with each other and point to its significance. A local volume fraction of ν = 40% was compared to a higher or lower value ν = 50% / ν = 35% to fit simultaneously a broad microporous signal as it is occurring in the Ni-system and a broad mesoporous signal, as it is occurring in the Mg-system (SI: Figure S11 and Figure S12). Even by adjusting the fitting parameters and considering different models, a single model which fits all occurring meso- and microporous features precisely is highly challenging to implement. As mentioned before the hard-sphere model considers sphere-like pore/particle and their interactions, but during the heating procedure the shape of the pores can change due to agglomeration or condensation, and the

development of interconnectivity. Therefore, a hard-cylinder or hard-worm model would take this population better into account, but it would neglect the sphere-like population. On the other hand, a composite model with two or more models implemented could give insignificant results as the contribution of each pore population to the overall SAXS signal is hard to distinguish. Consequently, we suggest that the used hard-sphere model is a reasonable compromise. Macroporous populations of pores in different systems were not considered in the fitting model as the q-range, with a minimum q-value of q_{min} = 0.138 nm^{-1}, approximated with $2\pi/q_{min} \approx 46$ nm pore/particle size, is not broad enough to cover these large features at low q. They are probably present in minor amounts. However, the micro-to-mesoporous signal is significant due to a fitting q-range and can be evaluated quantitatively.

Supplementary Note 2: Description of K-edge EXAFS spectra in R-space

After converting to an amorphous state, the distortion in the nickel phosphate phase remained practically unchanged. The crystalline Ni-struvite (t = 0 min), t = 10 min and t = 20 min samples show the most intense white line and the lowest pre-peak area compared to crystalline Ni-dittmarite and the longer heated (t = 40-150 mins) which exhibit a higher pre-peak intensity and a less intense white line (SI: Figure S14, Table S7). After Fourier transformation of χ(k) into R-space radial distances from the absorber atom can be compared between the samples. At around R ≈ 1.9 Å all samples display a maximum which is related to the single scattering path of the Ni-O or Co-O bond length. A significant peak at R of ≈2.7 Å can be observed in the longer heated samples (t = 40, 60, 90, 120 and 150 mins) and in NID which is absent in the Ni-struvite and the shorter heated samples (10 and 20 min). At R > 3.2 Å the precursor Ni-struvite and the briefly heated samples exhibit a much broader peak while NID and the longer heated samples demonstrate a significant signal around 3.7 Å. The spectra of the longer heated samples are mostly congruent with the crystalline NID pattern except for intensity changes. Up to the t = 20 min sample, Ni-struvite crystal structure was the best starting model, while the Ni-dittmarite crystal structure was more suitable for good fitting results for the samples with longer heating times (t = 40-150 min) (Figure S13). Based on these observations it is suggested that the amorphous phase which forms at 90°C from precursor Ni-struvite has a similar structure to NID. Indicators of this theory are the agreement of the fit results with NID after 20 mins as well as the χ(R) distances with the congruent patterns. Crystalline Ni-dittmarite was synthesized in a hydrothermal cell in saturated H_2O atmosphere from precursor Ni-struvite heated at 90°C. Therefore, it is only plausible that Ni-struvite decomposes in a dry environment also to a component similar to Ni-dittmarite, but in an amorphous state with no permanent long-range order.

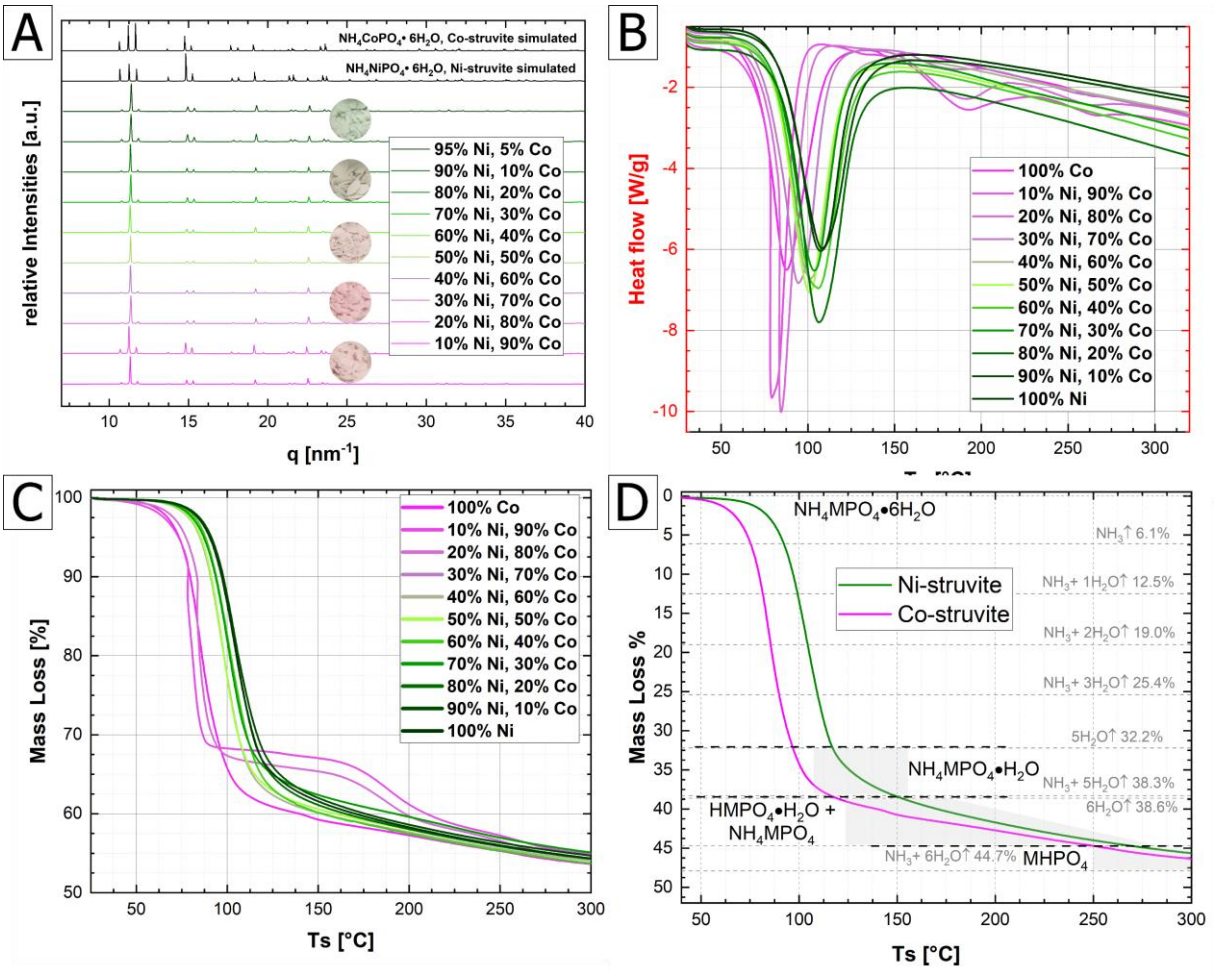

Figure S1: (A) Stacked XRD diagrams of synthesized Ni_xCo_{1-x}-struvite with photographs in circles of corresponding powder samples; Single-phase M-struvite was obtained in all samples with metal dependent greenish to pink color. (B) DSC measurements of Ni_xCo_{1-x}-struvite with x = 0-1 mixtures from 25°C-300°C with a heating rate of 10°C min^{-1}; Ni_xCo_{1-x}-samples below Ni# of 0.3 show similar to the pure Co-struvite samples two additional endothermic degassing peaks in DSC indicative for phase transitions; (C) TGA curves of Ni_xCo_{1-x}-struvites with Co-rich samples show distinct mass loss steps indicative for crystalline phase transition; (D) TGA graphs for the pure Ni and Co-struvite with the predicted mass loss (grey labels) and phase compositions (black labels).

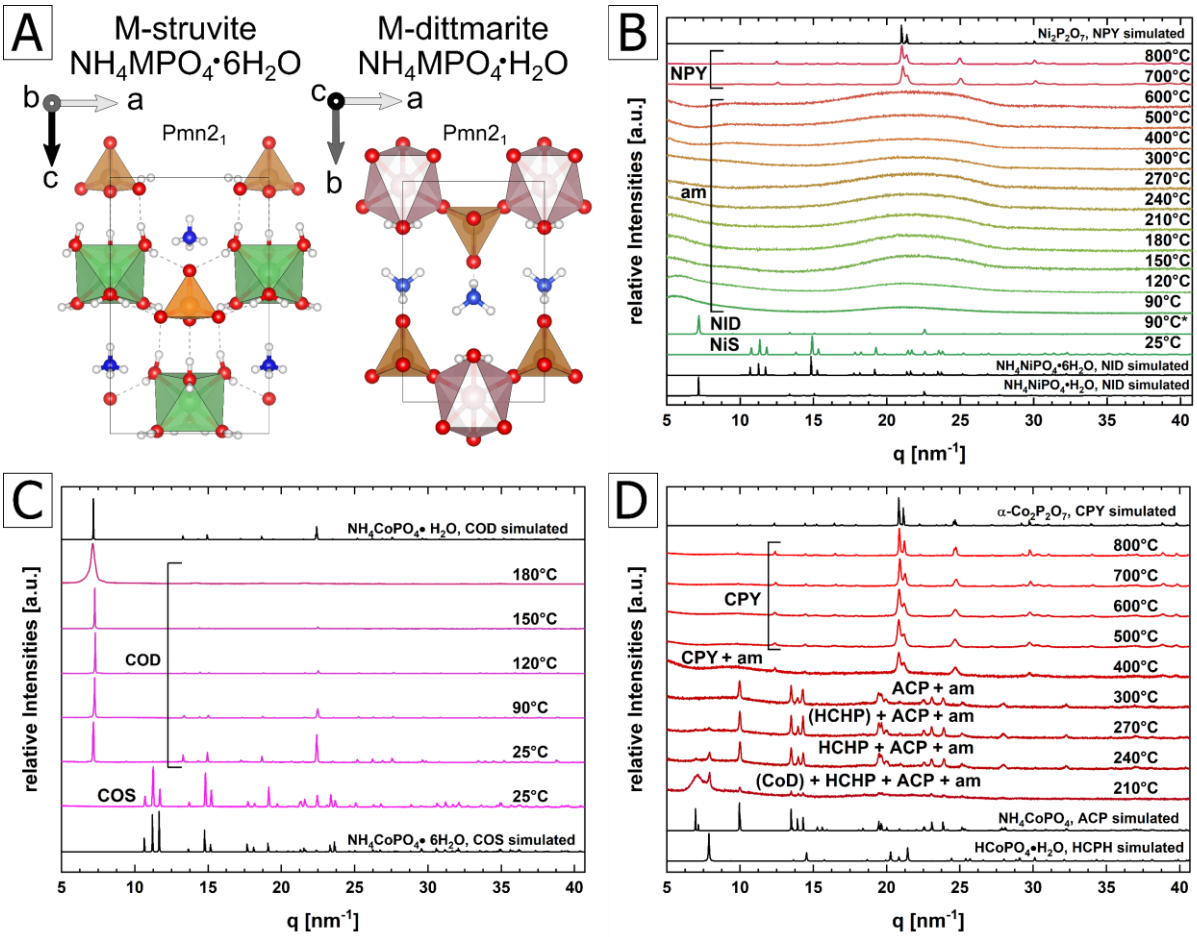

Figure S2: (A) Comparison of Crystal structures between M-struvite and M-dittmarite (both $Pmn2_1$); Stacked XRD patterns of thermally treated (B) Ni-struvite and (C,D) Co-struvite at different temperatures 25-800°C; While the Ni-containing phosphates remain amorphous until 600°C, the Co-bearing phosphates exhibit multiple crystalline phase transitions in this temperature range, abbreviations used Ni-struvite (NiS) reference database ICSD 403058; α-$Ni_2P_2O_7$ (NPY) reference ICSD 403058; Co-struvite reference ICSD 170042; Co-dittmarite (COD) COD reference database 2008122; α-NH_4CoPO_4 (ACP) PDF database reference 00-018-0402; Hydrogen cobalt(II)phosphate hydrate (HCPH) reference database ICSD 33828; α-$Co_2P_2O_7$ (CPY) reference database ICSD 280959.

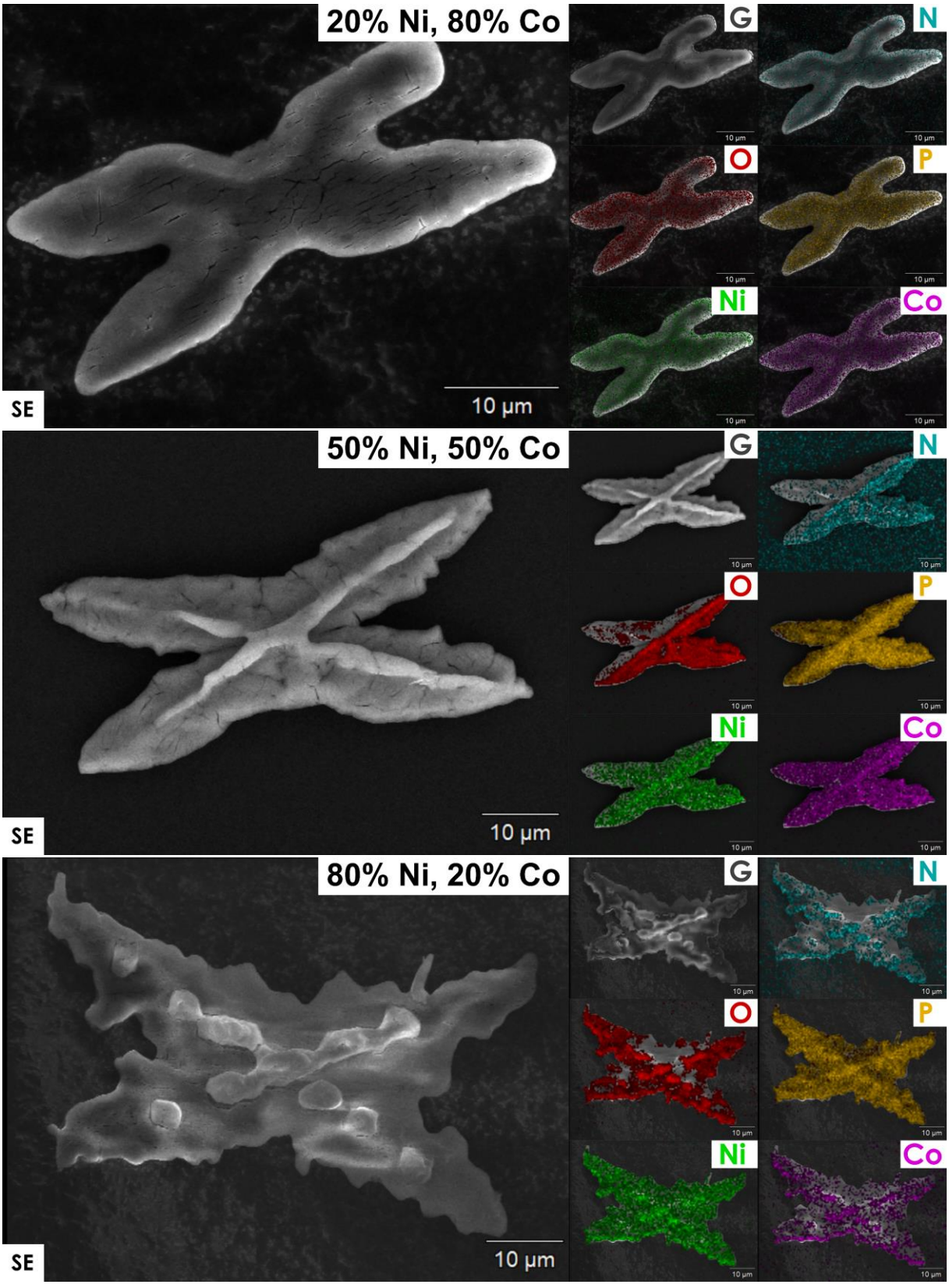

Figure S3: Selected EDX mappings of Ni_xCo_{1-x}-struvite crystals (x = 0.2, 0.5, 0.8) synthesized by mixing of 100 ml 0.02 M M^{2+}, M = c(Ni^{2+}+Co^{2+}) and 0.1 M DAP with the SE image on the left and the respective elements on the right (G: absolute intensity of counts in the EDX detector, N: nitrogen, O: oxygen, P: phosphorus, Ni: nickel and Co: cobalt); In the precursor Ni_xCo_{1-x}-struvites both metals are homogenously distributed. Shadows in the elemental maps are caused by roughness and topography of the crystals, deviating from a flat surface.

Figure S4: SE images of Mg-, Ni – and Co -struvite and their thermally-processed derivates at given temperatures (90°C, 120°C, 150°C); an overview image at a low magnification, marked with 1 and a detailed view at an individual crystal, marked with 2; (A) M-struvite as synthesized at room temperature; (B) M-struvite isothermally-heated at T=90°C for t = 1 d; (C) Mg- and Ni-struvites isothermally-heated at T=120°C for t = 1 d; (D) Mg- and Ni-struvites isothermally-heated at T=150°C for t = 1 d; (E) Ni-struvite isothermally heated for t = 1 d in a 100% H_2O environment (hydrothermal synthesis). While amorphous Ni-containing phosphates mimic the relict crystalline Ni-struvite morphology, except the hydrothermal sample, the Co-phosphates change their crystalline habit due to multiple crystalline phase transitions.

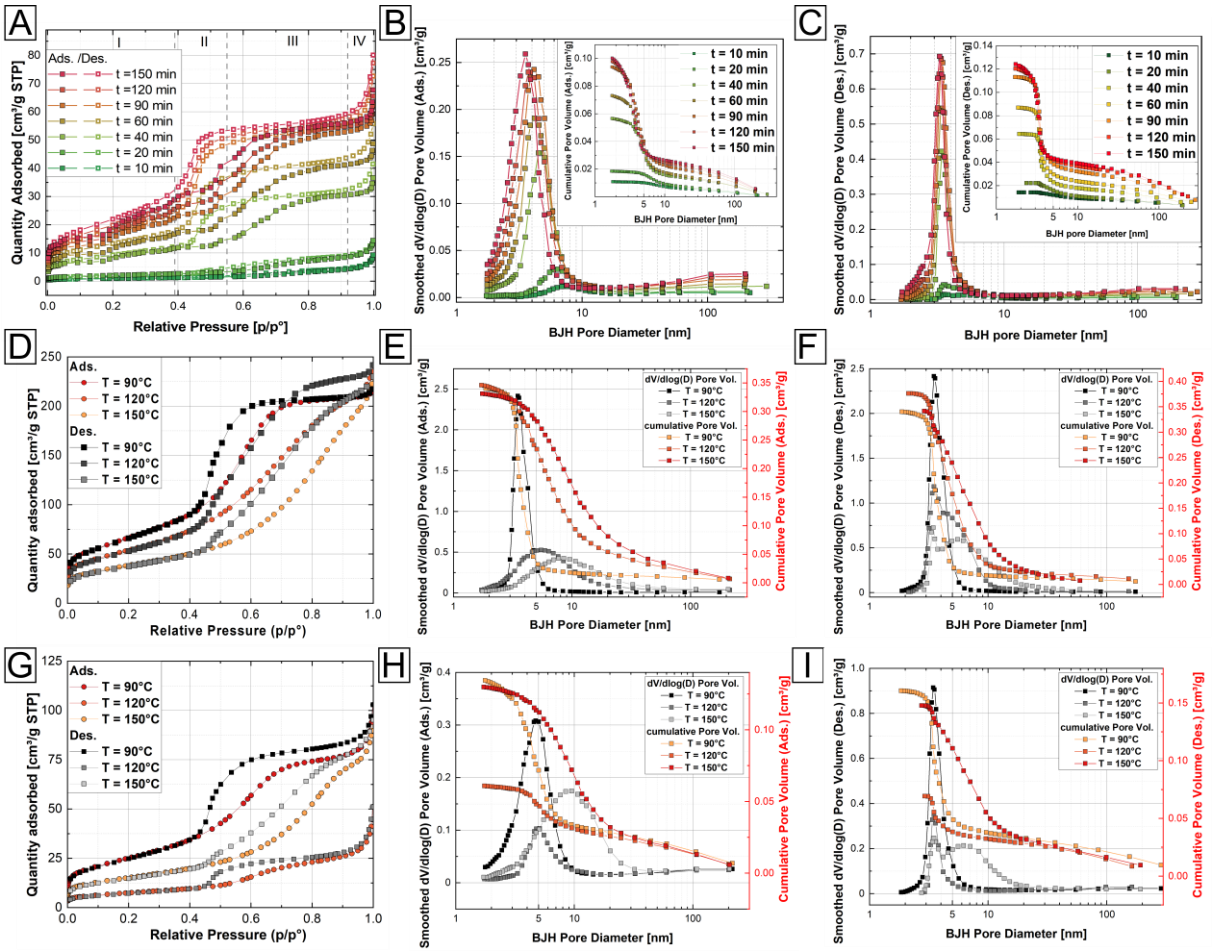

Figure S5: N_2 adsorption/desorption measurements of thermally treated Mg and Ni-struvite at T = 90°C , 120°C and 150 °C for t = 1 d and Ni- time-series (t = 10-150 min); (A) adsorption/desorption isotherms of heated Ni-struvite from t = 10 – 150 min; (B) average adsorption and (C) desorption BJH pore size change (dV/dlog) pore volume with insets of cumulative pore volume of adsorption/desorption, respectively; (D) adsorption/desorption isotherms of heated Mg-struvite T = 90°C, 120°C and 150°C indicating type IV hysteresis loops; (E) average adsorption and (F) desorption BJH pore size change (dV/dlog) pore volume with the cumulative pore volume, respectively;(G) adsorption/desorption isotherms of heated Ni-struvite indicating type IV hysteresis loops; (H) average adsorption and (I) desorption BJH pore size change (dV/dlog) pore volume with cumulative pore volume, respectively. With higher heating times and lower processing temperature, the BET surface area increases while the BJH pore size decreases significantly.

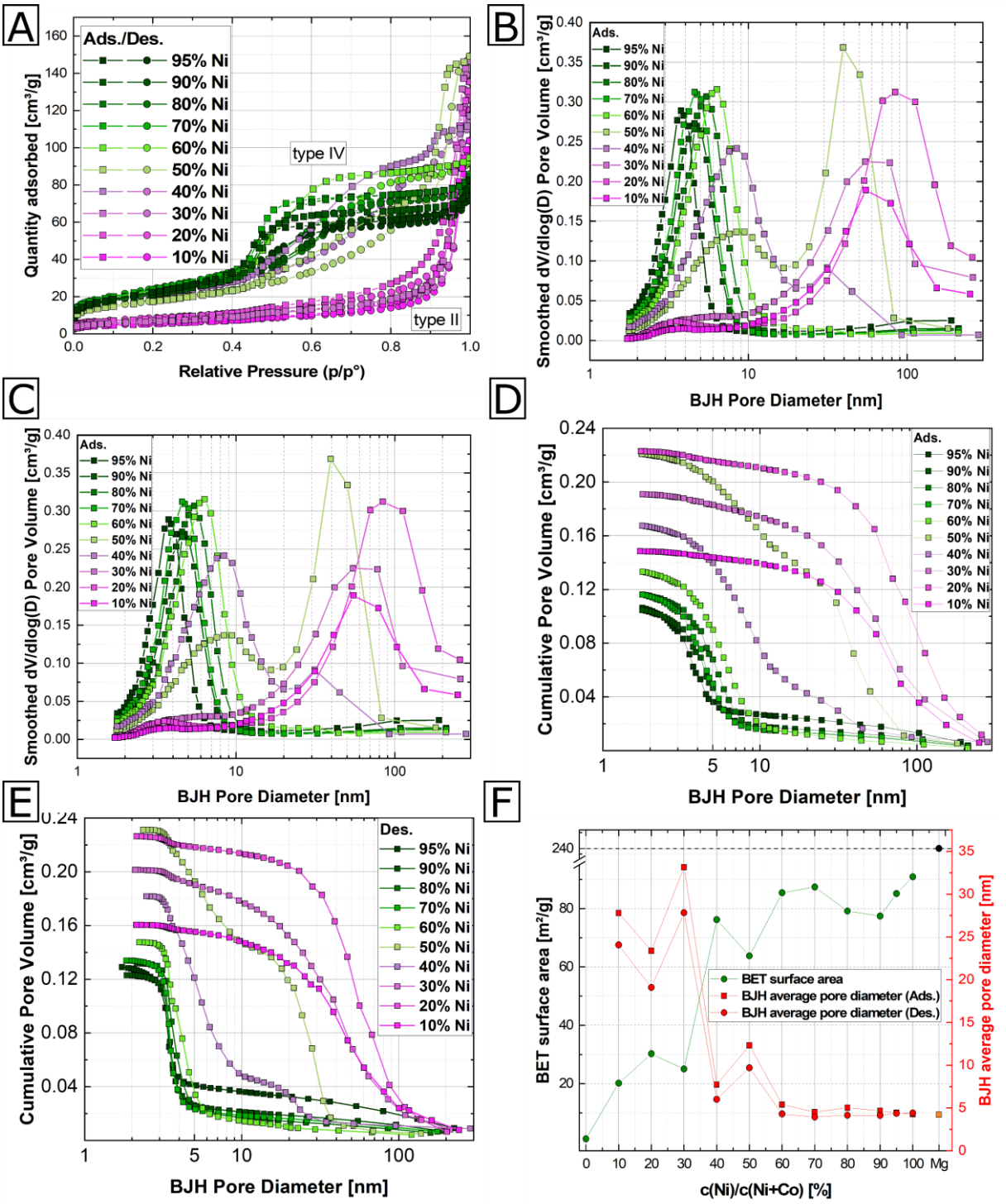

Figure S6: N_2 adsorption/desorption measurements of thermally-treated Ni_xCo_{1-x}-struvite at 90°C (A) adsorption/desorption isothermes of Ni_xCo_{1-x} solid solution; Note the evolution of type II to type IV isotherms with increasing Ni content;(C) average adsorption BJH pore size change (dV/dlog(D)) Pore volume; (D) average desorption BJH pore size change (dV/dlog(D) Pore volume; note the pore size changes in the adsorption/desorption BJH pore sizes with increasing Ni content;(E) adsorption and (F) desorption cumulative pore volume and (F) evolution of BET surface area [m^2/g] (green circles) and average ads./des. BJH pore diameter (red circles/squares) with increasing Ni-content of thermally treated Ni_xCo_{1-x} struvites and a pure Mg-struvite sample on the right side for comparison (black circle, orange square). With higher Ni-content in the Ni_xCo_{1-x}-mixtures, the absolute BET surface area increases and the BJH pore size decreases significantly.

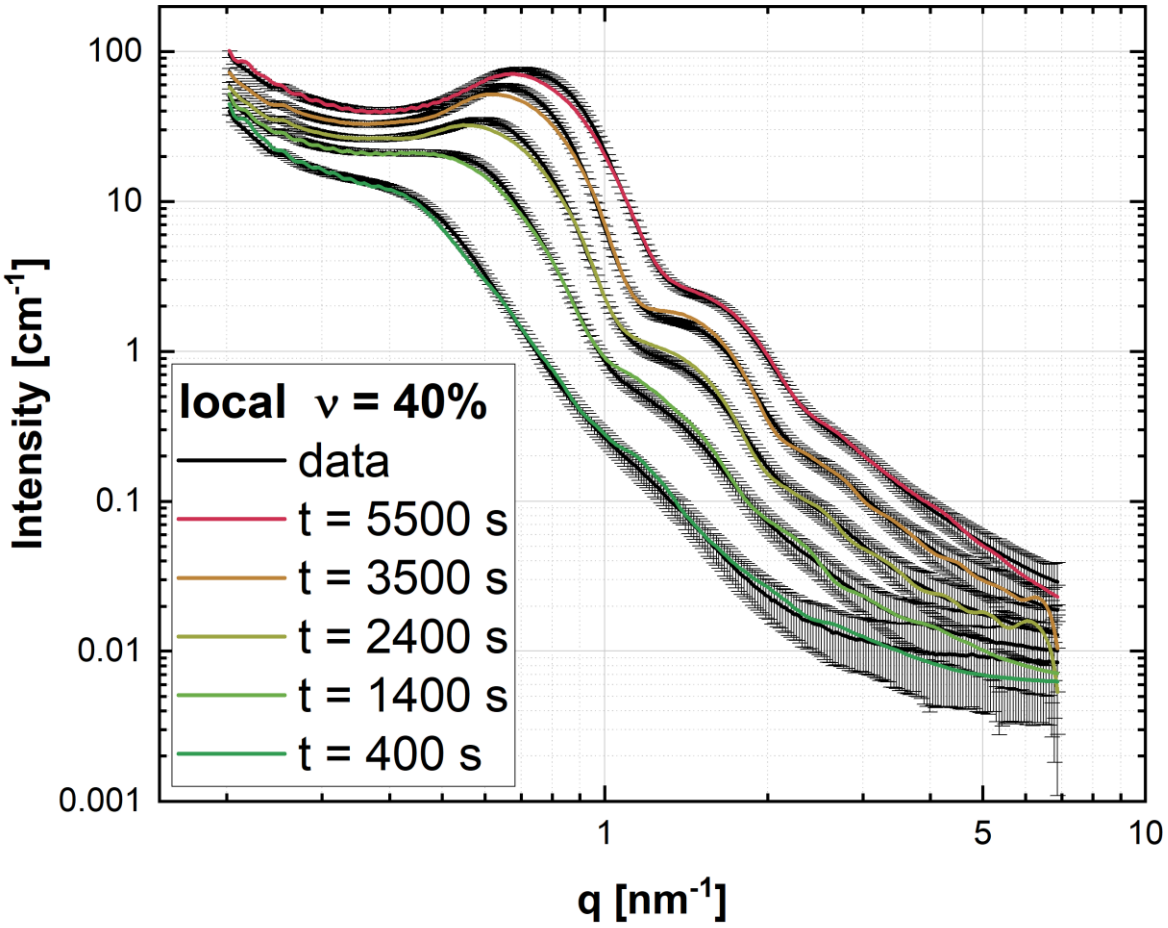

Figure S7: Selected McSAS fits of isothermally heated Mg-struvite at 90°C with a fixed local volume fraction ν = 40%; Fits of time steps t = 400 s, t = 1400 s, t = 2400 s, t = 3500 s and t = 5500 s are shown, black lines = data with error bars, colored lines = fits; The fits are in agreement with the data within the error bars. The mesoporous structures evolve with progressive heating visible in the occurrence of distinct SAXS scattering signal at low q (< 5nm^{-1}).

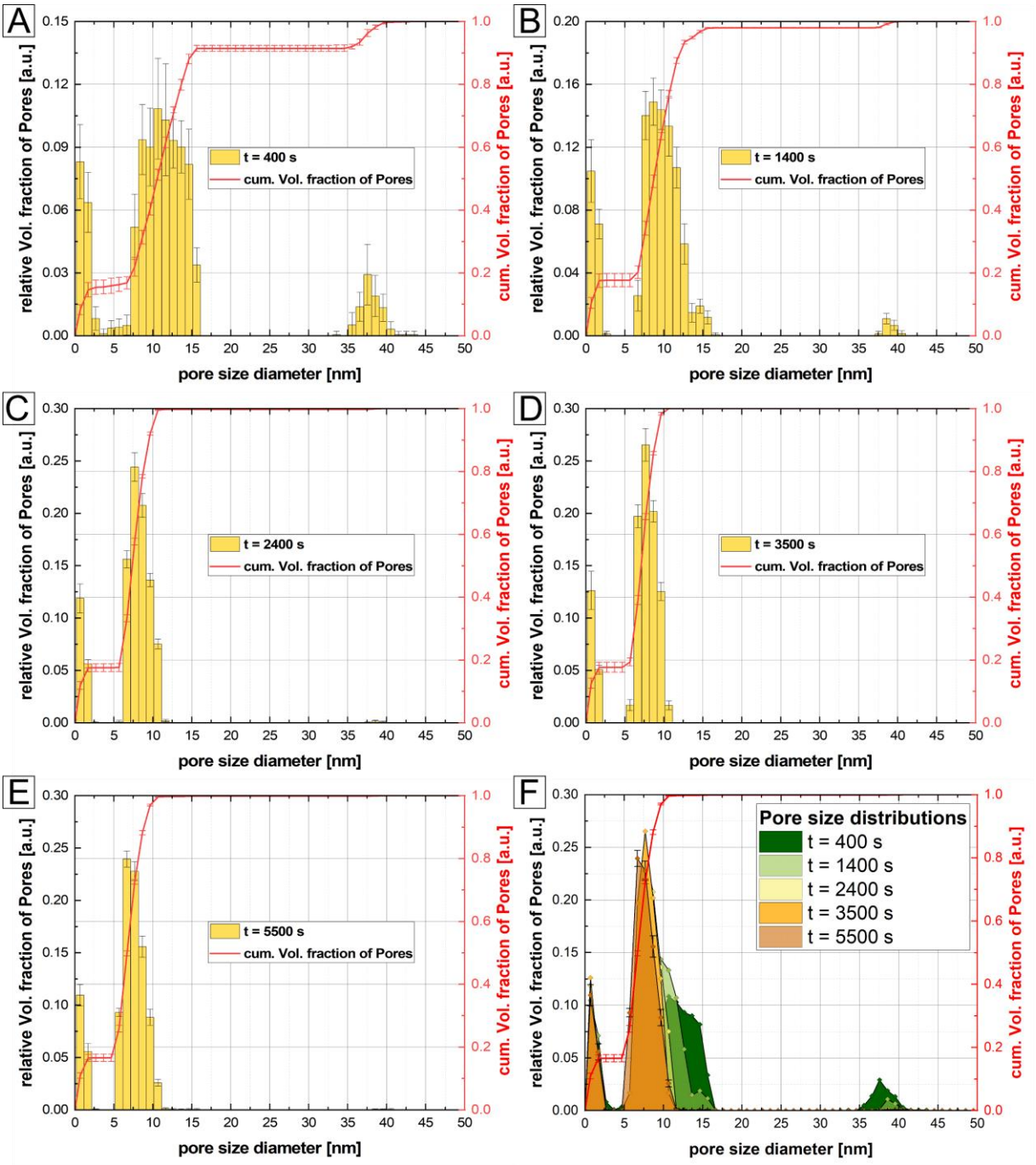

Figure S8: Selected pore size distribution histograms derived from McSAS fits of isothermally heated Mg-struvite at 90°C with a fixed local volume fraction of ν = 40; (A) fit of time step t = 400 s; (B) fit of time step t = 1400 s; (C) fit of time step t = 2400 s; (D) fit of time step t = 3500 s; (E) fit of time step t = 5500 s; (F) pore size distributions of all selected time steps (colored area below the curves) in the Mg-system with a fixed local volume fraction ν = 40% combined; error bars of only the final pore size distribution are added. With higher heating times, the pore size distribution becomes narrower time and the average pore size decreases.

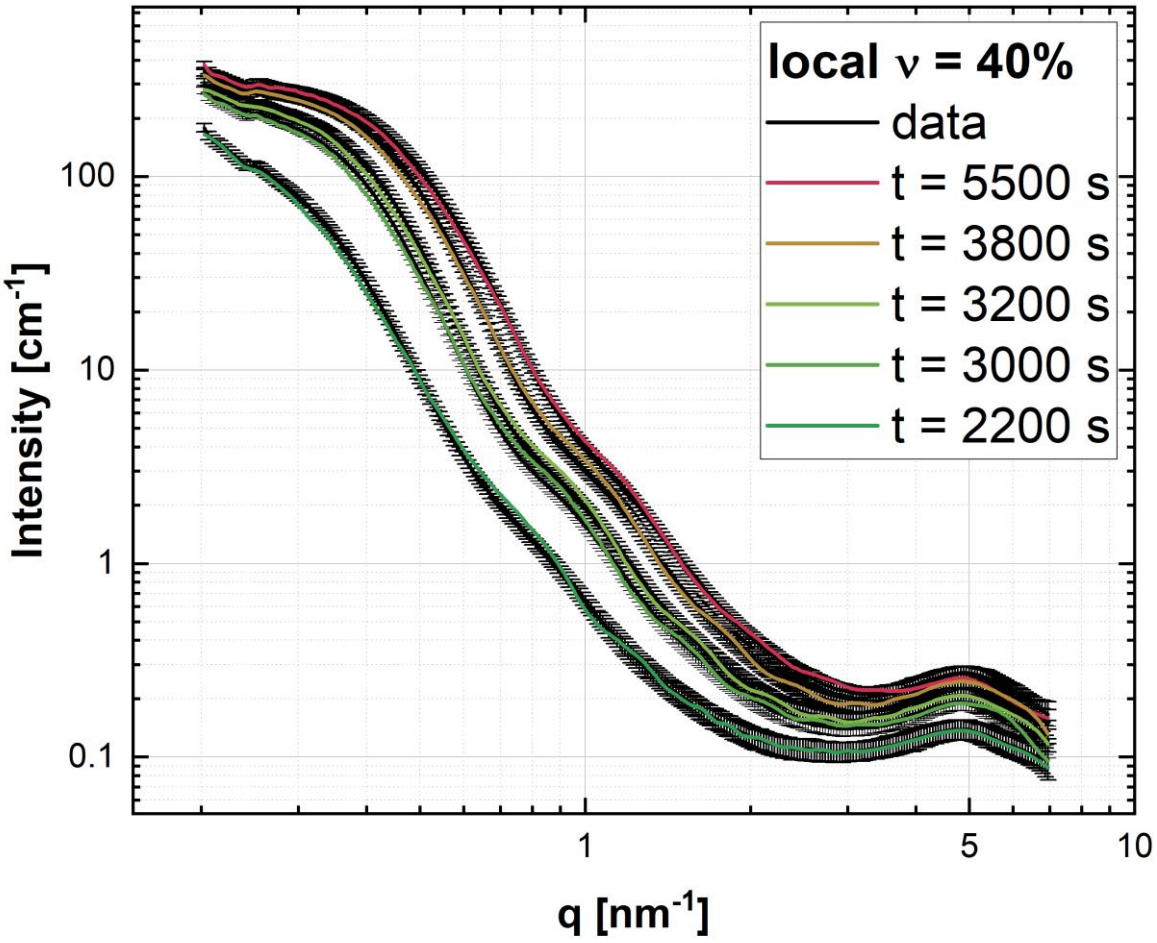

Figure S9: Selected McSAS fits of isothermally heated Ni-struvite at 90°C with a fixed local volume fraction ν = 40%;It was fitted not before t = 2000 s as in the Ni-system the mesoporous frameworks evolve much later than in the Mg-system; Fits of time steps t = 2200 s, t = 3000 s, t = 3200 s, t = 3800 s and t = 5500 s are shown, black lines = data with error bars, colored lines = fits; The fits are in agreement with the data within the error bars. Meso- and Microporosity evolves in the Ni-system with progressive heating visible in the occurrence of SAXS scattering signal at low (< 5nm^{-1}) and high q (around 5 nm^{-1}).

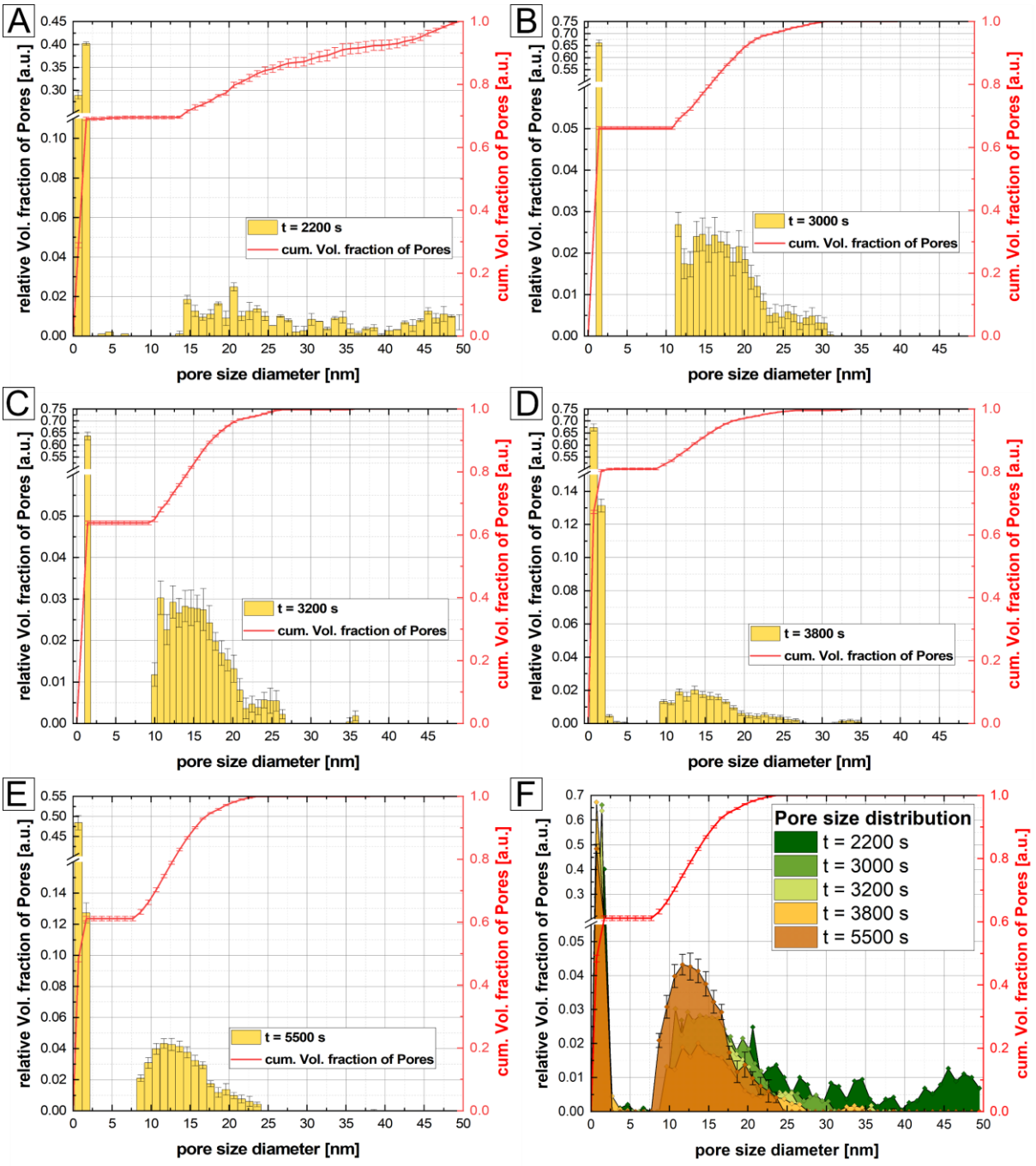

Figure S10: Selected pore size distribution histograms derived from McSAS fits of isothermally heated Ni-struvite at 90°C with a fixed local volume fraction of ν = 40; It was fitted not before t = 2000 s as in the Ni-system the mesoporous frameworks evolve much later than in the Mg-system; (A) fit of time step t = 2200 s; (B) fit of time step t = 3000 s; (C) fit of time step t = 3200 s; (D) fit of time step t = 3800 s; (E) fit of time step t = 5500 s; (F) pore size distributions of all selected time steps (colored area below the curves) in the Ni-system with a fixed local volume fraction ν = 40% combined; error bars of only the final pore size distribution are added. With higher heating times, the pore size distribution becomes more narrow and the average pore size decreases.

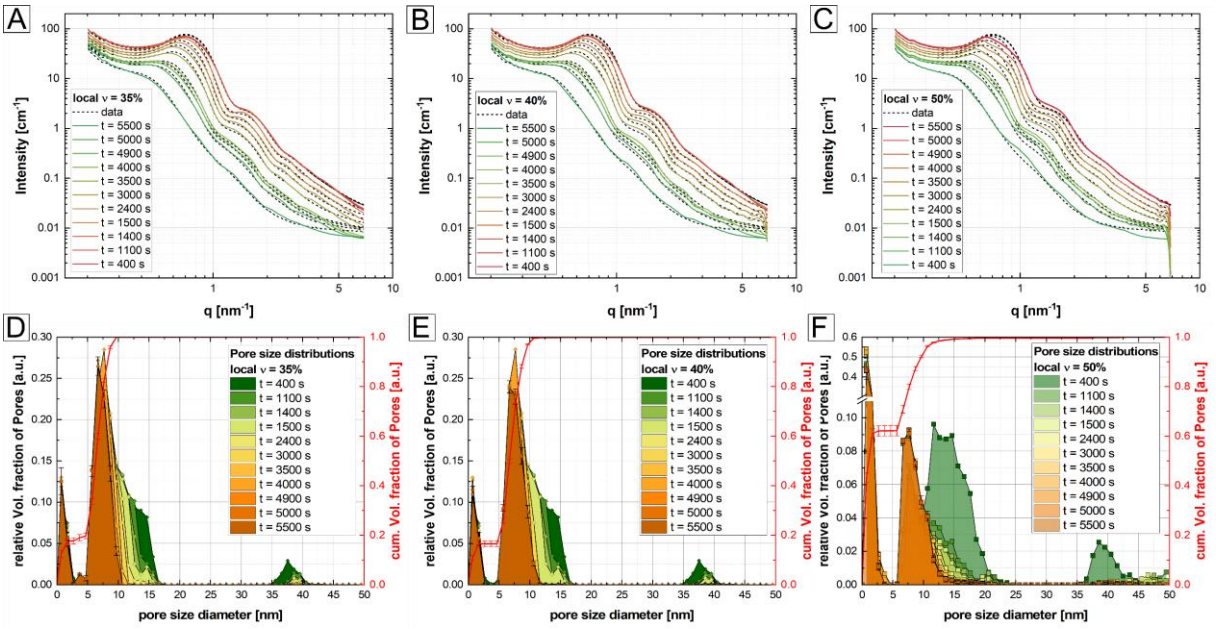

Figure S11: McSAS fits for isothermally heated Mg-struvite at 90°C with different local volume fractions (ν = 35%, 40% and 50%) and the resulting pore size distribution (relative volume fraction of pores); (A) McSAS fits for ν = 35%; (B) McSAS for ν = 40%; (C) McSAS fits for ν = 50%; (D) resulting pore size distribution from (A); (E) pore size distribution from (B); (F) pore size distribution from (C). A local volume fraction of ν = 40% provided the best fitting results as it is also in agreement with the BET data.

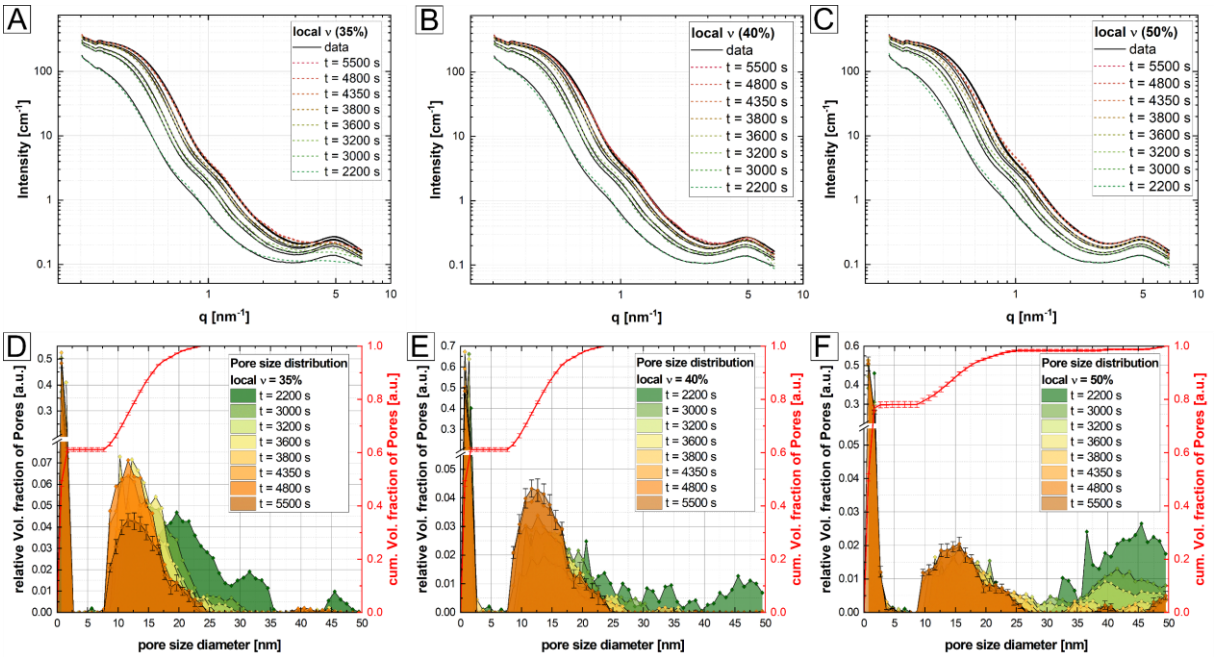

Figure S12: McSAS fits for isothermally heated Ni-struvite at 90°C with different local volume fractions (ν = 35%, 40% and 50%) and the resulting pore size distribution (relative volume fraction of pores); (A) McSAS fits for ν = 35%; (B) McSAS for ν = 40%; (C) McSAS fits for ν = 50%; (D) resulting pore size distribution from (A); (E) pore size distribution from (B); (F) pore size distribution from (C). A local volume fraction of ν = 40% provided the best fitting results as it is also in agreement with the BET data.

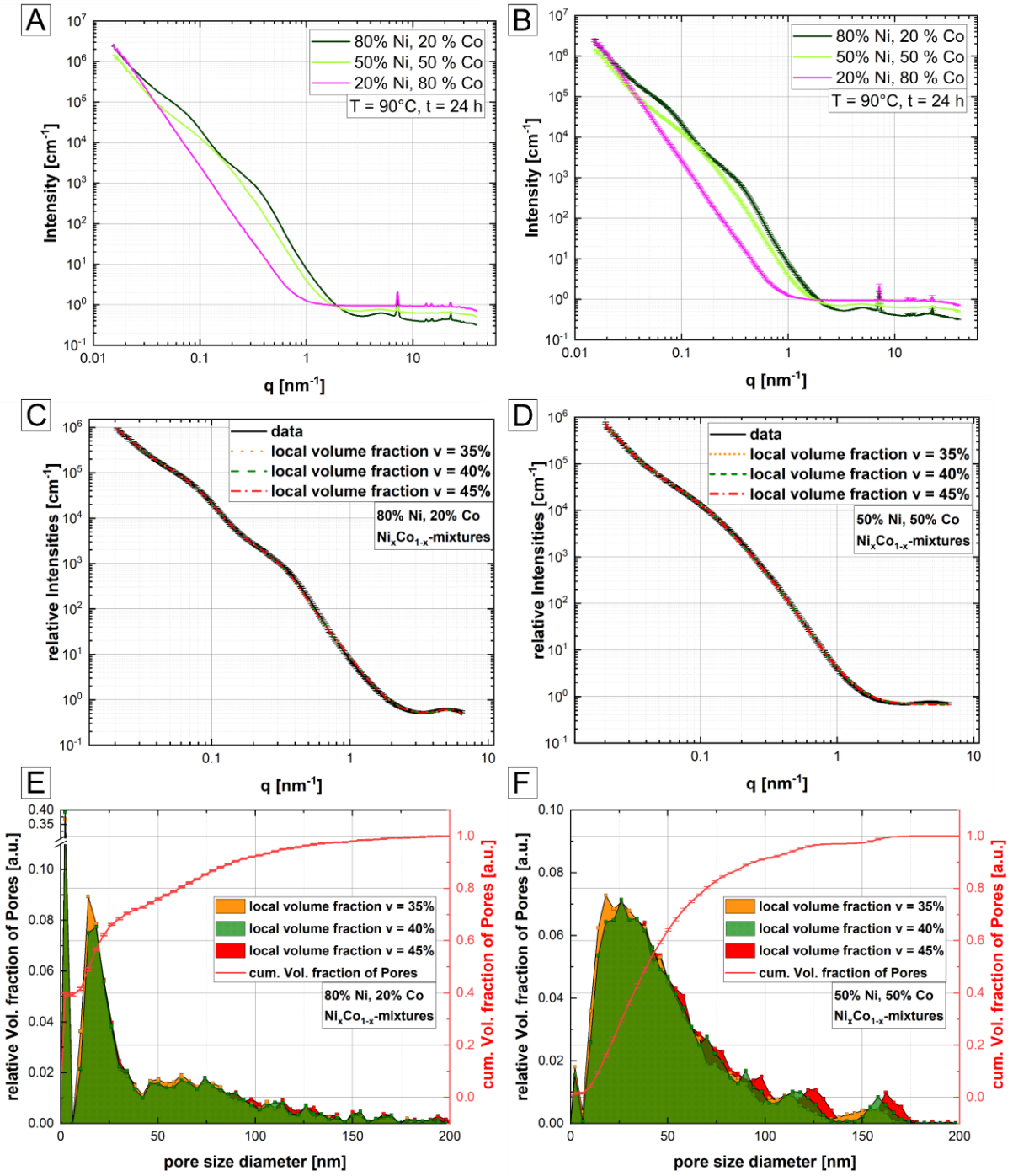

Figure S13: (A) Ex-situ SAXS/WAXS measurements of isothermally heated Ni_xCo_{1-x}-struvite with x = 0.2, 0.5, 0.8 at T = 90°C for t = 24 h and (B) data error bars; (C, D) McSAS fits with different local volume fractions of ν = 35%, 40% and 45% and (E,D) resulting pore size distribution of heated Ni_xCo_{1-x}-struvite with x = 0.5 and 0.8; The cumulative volume fraction is added from the fit with ν = 40%. The Ni-rich Ni_xCo_{1-x}-mixtures (x = 80%, 50%) showed significant mesoporosity visible in a scattering signal at low q while the Co-rich one demonstrated no significant scattering in this q-region.

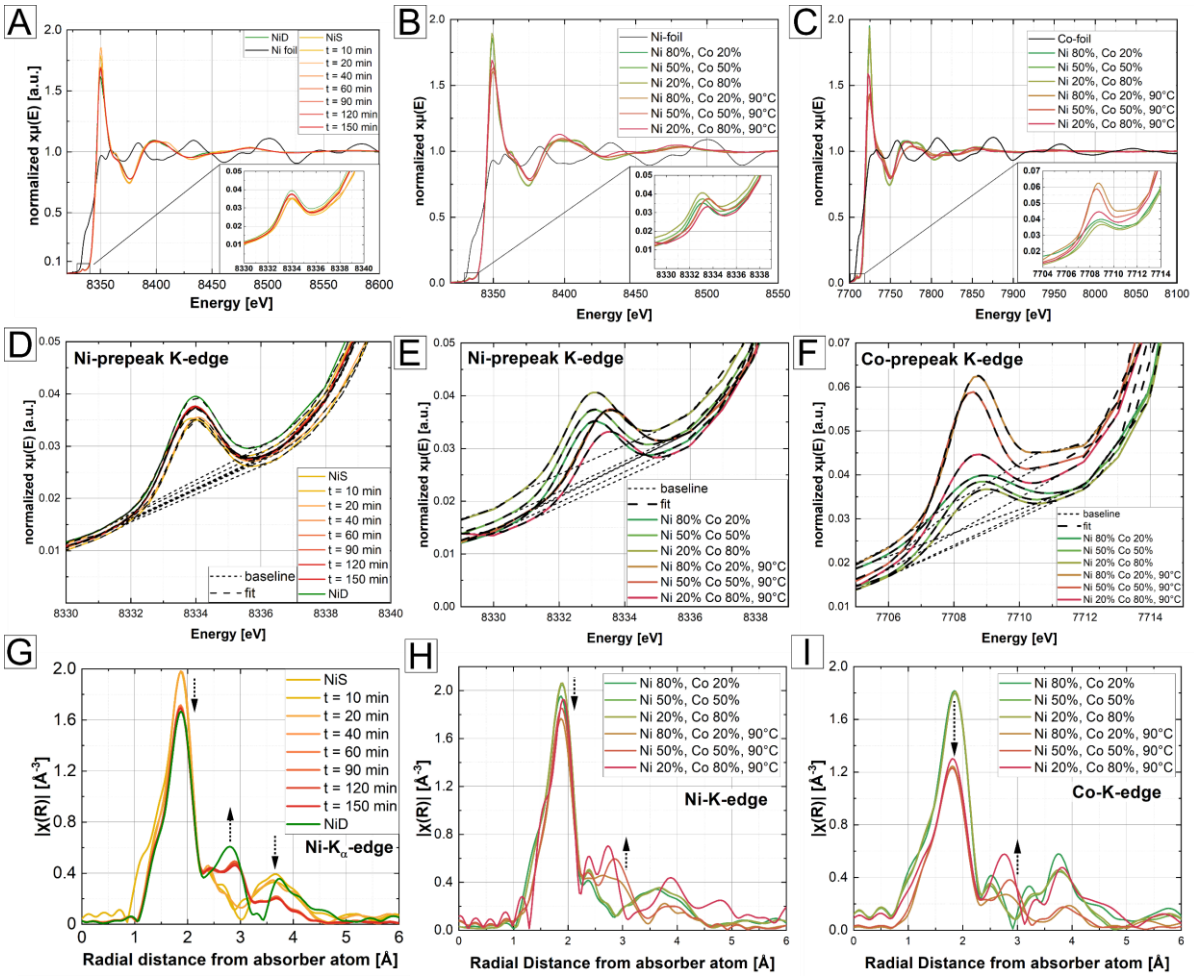

Figure S14: Ni- and Co-K-edge XAS spectra of (A) Ni-time series (NiS, t = 10 min, 20 min, 40 min, 60 min, 90 min, 120 min, 150 min, NiD), (B-C) crystalline precursor Ni_xCo_{1-x}-struvites (x = 0.2, 0.5, 0.8) and their heated products with detailed window on pre-peak region; Quantitative pre-peak fits with a Gaussian function model of (D) the Ni-time series and (E-F) of Ni_xCo_{1-x} mixtures in both absorption edges (Ni- and Co- K-edge); all integration results are summarized in Table S8Table S9; Fourier-transformed Ni- and Co spectra plotted in R-space of (G) Ni-time series and (H-I) of Ni_xCo_{1-x} mixtures in both absorption edges (Ni- and Co- K-edge). While Ni is in all processed Ni_xCo_{1-x}-mixtures similarly distorted, Co shows a high degree of distortion in the Ni-rich samples.

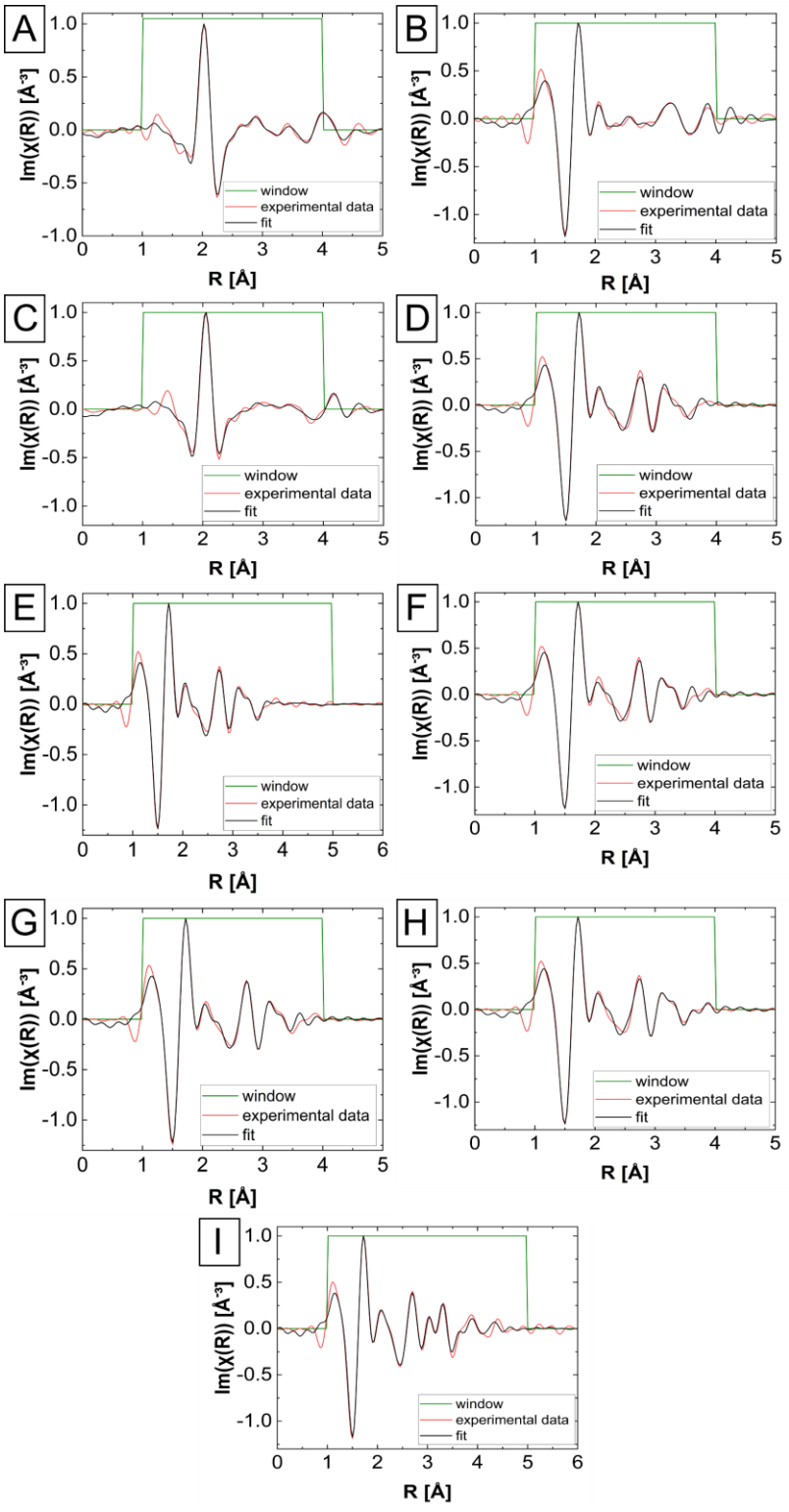

Figure S15: Fits Ni- K-edge EXAFS data shown in real space of isothermally heated Ni t-series at 90°C for (A) Ni-struvite at 25°C, R = 0.011; (B) t = 10 min, R = 0.008; (C) t = 20 min, R = 0.009; (D) t = 40 min, R = 0.011; (E) t = 60 min, R = 0.013; (F) t = 90 min, R = 0.008; (G) t = 120 min, R = 0.010, (H) t = 150 min, R = 0.009; (I) hydrothermally synthesized crystalline Ni-dittmarite, R = 0.012. The fits are mainly in agreement with the data visible in the fitting parameters.

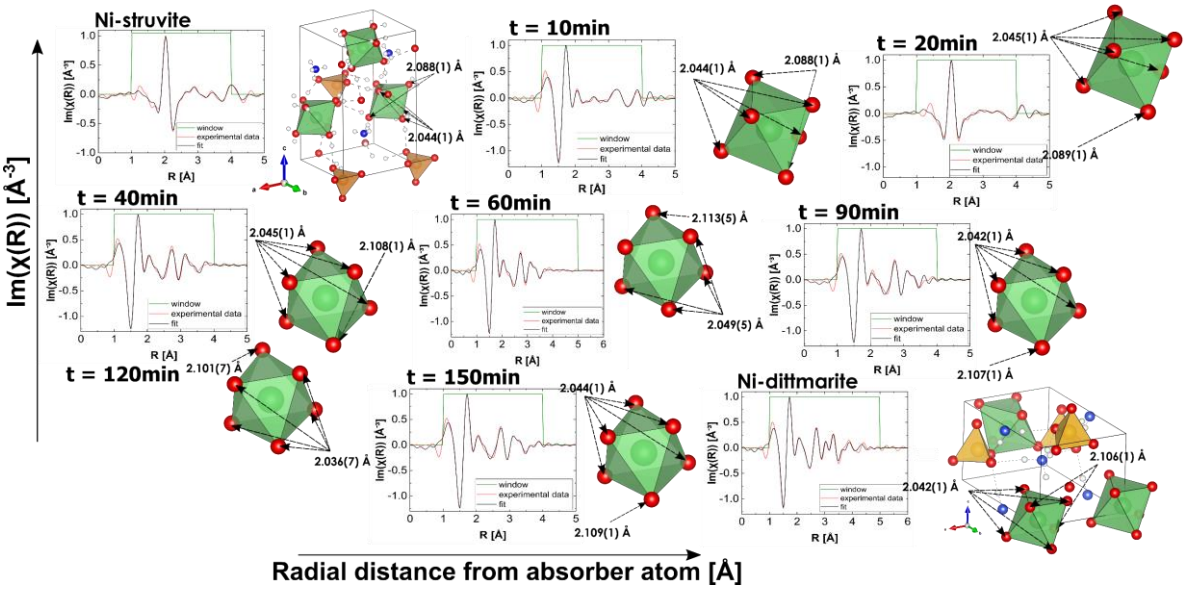

Figure S16: Ni K-edge EXAFS data shown in real space for crystalline precursor Ni-struvite $NH_4NiPO_4{\cdot}6H_2O$ space group: $Pmn2_1$, time series 10-150 min and hydrothermally synthesized crystalline Ni-dittmarite $NH_4NiPO_4{\cdot}H_2O$ space group: $Pmn2_1$ with corresponding bond distances marked in the crystal structure; Note how the coordination environment changes t = 10-40 min.

Equations

$$S_c(q) = (1 + 24\nu G(2qR_{HS})/(2qR_{HS}))^{-1} \quad \text{Eq. [S1]}$$

$$\begin{aligned} G(2qR_{HS}) = {} & \alpha[sin(2qR_{HS}) - (2qR_{HS})cos(2qR_{HS})](2qR_{HS})^{-2} \\ & + \beta[2(2qR_{HS})sin(2qR_{HS}) + (2 - (2qR_{HS})^2)cos(2qR_{HS}) \\ & - 2](2qR_{HS})^{-3} + \gamma[-(2qR_{HS})^4 cos(2qR_{HS}) \\ & + 4[3(2qR_{HS})^2 - 6]cos(2qR_{HS}) \\ & + 4[((2qR_{HS})^3 - 6(2qR_{HS})]sin(2qR_{HS}) + 24](2qR_{HS})^{-5} \end{aligned}$$

$$\alpha = \frac{(1+2\nu)^2}{(1-\nu)^4}$$

$$\beta = \frac{-6\nu\left(1+\frac{\nu}{2}\right)^2}{(1-\nu)^4}$$

$$\gamma = \frac{\nu\alpha}{2}$$

Equation S1: Full explanation of the Percus-Yevick structure factor[5] with only two free variables: the hard sphere radius R_{Hs} and the local volume fraction ν; all other parameters G, α, β, γ are dependent on these two.

$$V_{pores} = \nu_{BJH} \cdot m_{total}; \qquad V_{total} = \frac{m_{total}}{\rho_{bulk}}; \qquad \varphi_{pores} = \frac{V_{pores}}{V_{total}};$$

$$\varphi_{pores,Mg-struvite} = \frac{0.328\ cm^3 g^{-1} \cdot 0.319\ g}{\frac{0.319\ g}{1.3\ g\ cm^{-3}}} = 0.425 \approx 40\ \% \quad \text{Eq. [S2]}$$

Equation S2: Calculation of the approximated volume fraction of pores in Mg-struvite from BET N2 adsorption/desorption data; ϕ_{pores} = volume fraction of pores; V_{pores} = volume of pores [cm³]; m_{total} = total mass of substance [g]; V_{total} = total volume of substance [cm³]; ν_{BJH} = specific volume of pores per mass [$cm^3 g^{-1}$]; ρ_{bulk} = bulk density of substance [g/cm^3].

Table S1: DSC integration results in Figure 1 (the main text) and Figure S1 by using a Pseudo Voigt function with χ^2, R^2 value, centroid and onset temperature of the endothermic DSC peak.

	TGA/DSC integration results				**fit function: Pseudo-Voigt**		
Sample	Peaks	χ^2	R^2	Onset T [°C]	Centroid T [°C]	FWHM	Max. Height
Mg-struvite	1	0.004	0.996	87.7	118.8	28.8	-6.2
Ni-struvite	1	0.003	0.994	83.0	113.3	26.2	-5.1
Co-struvite	1	0.004	0.993	72.4	91.8	20.7	-5.5
	2			136.2	150.5	19.5	-0.3
	3			249.2	271.3	21.2	-0.3
$Ni_{0.1}Co_{0.9}$-struvite	1	0.003	0.995	77.5	89.7	11.2	-8.5
	2			158.2	190.0	34.8	-0.8
	3			242.6	263.5	20.4	-0.2
$Ni_{0.2}Co_{0.8}$-struvite	1	0.010	0.987	78.2	90.8	12.2	-7.9
	2			155.4	186.8	31.2	-0.7
	3			238.2	259.5	27.5	-0.2
$Ni_{0.3}Co_{0.7}$-struvite	1	0.005	0.993	77.4	98.2	23.2	-5.7
	2			158.3	175.8	24.2	-0.2
	3			224.8	250.8	25.8	-0.1
$Ni_{0.4}Co_{0.6}$-struvite	1	0.003	0.993	79.2	106.2	25.4	-5.6
$Ni_{0.5}Co_{0.5}$-struvite	1	0.003	0.992	80.0	105.5	23.7	-5.6
$Ni_{0.6}Co_{0.4}$-struvite	1	0.003	0.996	80.1	110.0	28.0	--5.7
$Ni_{0.7}Co_{0.3}$-struvite	1	0.002	0.997	81.8	108.2	27.0	-6.1
$Ni_{0.8}Co_{0.2}$-struvite	1	0.001	0.998	81.5	104.6	26.7	-6.2
$Ni_{0.9}Co_{0.1}$-struvite	1	0.002	0.998	85.1	110.83	26.4	-5.8

Table S2: Summarized EDS data (Ni# = 0.1-0.95, A-H) from multiple mappings with weight and atomic percentage of the respective element; UDL = under detection limit; Sodium (Na), Sulphur (S), and Silicon (Si) were measured to evaluate the contamination of the samples and if the reactants completely reacted; Nitrogen as a volatile compound is in all mappings recorded but evaporated quickly (within seconds); Note the matching Ni# in solution and Ni# in the crystal.

A	Element	wt. %	SD	at. %	SD
c(Ni^{2+}) [mM] in solution	N K	0.2	0.4	0.3	0.7
2	O K	43.5	0.6	68.0	0.9
c(Co^{2+}) [mM] in solution	Na K	0.3	0.2	0.4	0.2
18	Si K	0.2	0.1	0.2	0.1
Ni# [%] in solution	P K	19.4	0.3	15.7	0.2
10.00	S K	UDL	UDL	UDL	UDL
Ni# [%] in crystal (EDX)	Co K	32.4	2.1	13.8	0.9
10.94	Ni K	4.0	1.1	1.7	0.5
number of mapped crystals		100.0		100.0	
4					

Table S2, continued:

B	Element	wt. %	SD	at. %	SD
c(Ni^{2+}) [mM] in solution	N K	UDL	UDL	UDL	UDL
4	O K	35.3	0.9	60.9	1.5
c(Co^{2+}) [mM] in solution	Na K	0.1	0.3	0.2	0.4
16	Si K	0.6	0.2	0.8	0.2
Ni# [%] in solution	P K	21.0	0.4	18.4	0.4
20.00	S K	0.2	0.3	0.1	0.3
Ni# [%] in crystal (EDX)	Co K	31.8	4.0	14.8	1.9
24.97	Ni K	11.0	2.4	4.9	1.1
number of mapped crystals		100.0		100.0	
4					

C	Element	wt. %	SD	at. %	SD
c(Ni^{2+}) [mM] in solution	N K	UDL	UDL	UDL	UDL
6	O K	38.6	0.7	63.7	1.1
c(Co^{2+}) [mM] in solution	Na K	0.1	0.2	0.1	0.2
14	Si K	1.2	0.1	1.1	0.1
Ni# [%] in solution	P K	20.4	0.4	17.4	0.3
30.00	S K	UDL	UDL	UDL	UDL
Ni# [%] in crystal (EDX)	Co K	27.6	2.5	12.4	1.1
30.48	Ni K	12.1	1.6	5.4	0.7
number of mapped crystals		100.0		100.0	
4					

Table S2, continued:

D	Element	wt. %	SD	at. %	SD
c(Ni^{2+}) [mM] in solution	N K	UDL	UDL	UDL	UDL
8	O K	30.4	0.6	55.6	1.1
c(Co^{2+}) [mM] in solution	Na K	0.3	0.2	0.3	0.3
12	Si K	0.3	0.1	0.3	0.1
Ni# [%] in solution	P K	20.9	0.3	19.8	0.3
40.00	S K	UDL	UDL	UDL	UDL
Ni# [%] in crystal (EDX)	Co K	29.4	2.4	14.7	1.2
39.05	Ni K	18.8	1.9	9.4	0.9
number of mapped crystals		100.0		100.0	
4					

E	Element	wt. %	SD	at. %	SD
c(Ni^{2+}) [mM] in solution	N K	UDL	UDL	UDL	UDL
10	O K	40.4	0.7	65.5	1.1
c(Co^{2+}) [mM] in solution	Na K	0.2	0.3	0.2	0.3
10	Si K	0.9	0.1	0.8	0.1
Ni# [%] in solution	P K	18.6	0.4	15.7	0.3
50.00	S K	0.0	0.2	0.0	0.1
Ni# [%] in crystal (EDX)	Co K	20.6	2.5	9.2	1.1
48.39	Ni K	19.3	2.0	8.6	0.9
number of mapped crystals		100.0		100.0	
4					

F	Element	wt. %	SD	at. %	SD
c(Ni^{2+}) [mM] in solution	N K	UDL	UDL	UDL	UDL
12	O K	34.7	6.7	59.7	7.1
c(Co^{2+}) [mM] in solution	Na K	UDL	UDL	UDL	UDL
8	Si K	0.1	0.2	0.1	0.1
Ni# [%] in solution	P K	21.2	1.2	19.1	2.5
60.00	S K	UDL	UDL	UDL	UDL
Ni# [%] in crystal (EDX)	Co K	16.7	2.0	7.9	1.6
62.26	Ni K	27.3	4.7	13.1	3.4
number of mapped crystals		100.0		100.0	
4					

Table S2, continued:

G	Element	wt. %	SD	at. %	SD
c(Ni^{2+}) [mM] in solution	N K	UDL	UDL	UDL	UDL
14	O K	35.4	0.6	60.6	1.0
c(Co^{2+}) [mM] in solution	Na K	0.1	0.2	0.2	0.2
6	Si K	0.3	0.1	0.3	0.1
Ni# [%] in solution	P K	21.2	0.3	18.8	0.3
70.00	S K	0.0	0.2	0.00	0.1
Ni# [%] in crystal (EDX)	Co K	12.4	1.5	5.8	0.7
71.32	Ni K	30.6	2.8	14.4	1.3
number of mapped crystals		100.0		100.0	
4					

H	Element	wt. %	SD	at. %	SD
c(Ni^{2+}) [mM] in solution	N K	UDL	UDL	UDL	UDL
16	O K	39.3	4.3	64.7	3.8
c(Co^{2+}) [mM] in solution	Na K	0.2	0.2	0.2	0.2
4	Si K	0.2	0.2	0.2	0.2
Ni# [%] in solution	P K	19.1	1.3	16.3	1.1
80.00	S K	0.0	0.0	0.0	0.0
Ni# [%] in crystal (EDX)	Co K	6.7	1.3	3.0	0.7
83.94	Ni K	34.6	4.4	15.7	3.0
number of mapped crystals		100.0		100.0	
4					

I	Element	wt. %	SD	at. %	SD
c(Ni^{2+}) [mM] in solution	N K	UDL	UDL	UDL	UDL
18	O K	36.1	1.0	61.6	1.7
c(Co^{2+}) [mM] in solution	Na K	0.3	0.4	0.4	0.5
2	Si K	0.3	0.2	0.2	0.2
Ni# [%] in solution	P K	19.6	0.6	17.3	0.5
90.00	S K	0.2	0.2	0.2	0.2
Ni# [%] in crystal (EDX)	Co K	5.1	2.1	2.3	1.0
88.59	Ni K	38.5	4.4	18.0	2.1
number of mapped crystals		100.0		100.0	
4					

Table S2, continued:

J	Element	wt. %	SD	at. %	SD
c(Ni^{2+}) [mM] in solution	N K	UDL	UDL	UDL	UDL
19	O K	34.6	1.2	59.8	2.1
c(Co^{2+}) [mM] in solution	Na K	0.3	0.5	0.4	0.6
2	Si K	0.4	0.3	0.3	0.3
Ni# [%] in solution	P K	20.4	0.7	18.4	0.6
95.00	S K	0.1	0.2	0.1	0.2
Ni# [%] in crystal (EDX)	Co K	2.9	2.1	1.4	1.0
93.51	Ni K	41.4	4.5	19.8	2.1
number of mapped crystals		100.0		100.0	
5					

Table S3: BET N_2 gas sorption results for the pure Mg-, Ni- and Co-struvites; The adsorption BJH pore volume was always used; Co-struvite shows no significant BET surface area resulting in no calculable meaningful BJH pore size could be calculated, indicated by (-).

struvite system	t [min]	T [°C]	BET surface area [$m^2\ g^{-1}$]	BJH pore volume [$cm^3\ g^{-1}$]	average BJH pore diameter [nm]
Ni t-series	10 min	90	3.61(1)	0.01	12.3
	20 min		7.46(1)	0.02	9.0
	40 min		34.3(2)	0.06	5.7
	60 min		48.7(2)	0.07	5.0
	90 min		64.9(3)	0.09	4.8
	120 min		73.2(5)	0.10	4.6
	150 min		90.4(5)	0.13	5.2
Mg	1d	90	240.5(9)	0.32	4.2
Ni	1d	90	85.8(4)	0.10	4.2
Co	1d	90	1.06(1)	(-)*	(-)*
Mg	1d	120	195.9(5)	0.35	7.6
Ni	1d	120	26.9(1)	0.06	8.3
Mg	1d	150	138.2(2)	0.33	8.3
Ni	1d	150	54.5(1)	0.13	8.4

Table S4: BET N_2 gas sorption results for the Ni_xCo_{1-x}-mixtures; the adsorption BJH pore volume was always used.

BET N_2 results	(Ni_xCo_{1-x})-mixtures	T = 90°C	T = 24 h
Ni#	BET surface area [$m^2\ g^{-1}$]	BJH pore volume [$cm^3\ g^{-1}$]	Ø average BJH pore diameter [nm]
10	20.1(2)	0.15	27.8
20	30.2(4)	0.19	23.4
30	25.0(2)	0.22	33.2
40	76.2(3)	0.17	7.7
50	63.8(1)	0.22	12.3
60	85.4(3)	0.13	5.4
70	87.4(5)	0.12	4.5
80	79.2(3)	0.12	5.0
90	77.5(4)	0.10	4.7
95	82.2(5)	0.11	4.4

Table S5: Calculated average pore sizes (diameters) of all pores and selected pore populations (micro- vs. mesopores) in heated Mg- and Ni-struvite from SAXS data; the transitional mesoporous population at early stages was excluded as it disappears after continuous heating.

SAXS fits		all pores		microporous population (0-2 nm)		Main mesoporous population (2-50 nm)	
	t[s]	μ (diameter) [nm]	σ [nm]	μ (diameter) [nm]	σ [nm]	μ (diameter) [nm]	σ [nm]
Mg	400	13.8	10.2	1.3	0.6	12.6	2.5
	1100	10.5	7.2	1.1	0.5	11.1	2.3
	1400	9.9	6.4	1.1	0.5	10.5	2.2
	1600	7.8	6.0	1.2	0.3	11.7	2.9
	2400	4.3	5.0	1.0	0.3	9.3	1.9
	2950	4.1	4.5	1.0	0.3	8.8	1.6
	3450	4.0	4.1	1.0	0.3	8.5	1.4
	4000	4.1	3.9	1.0	0.3	8.1	1.3
	4900	6.6	3.1	1.0	0.4	7.7	1.3
	4980	6.6	3.1	1.0	0.5	7.7	1.3
	5500	6.6	3.0	1.0	0.5	7.7	1.3
Ni	2200	15.1	12.0	1.0	0.4	21.8	5.8
	3000	6.8	8.3	1.0	0.2	18.1	5.0
	3200	4.3	6.9	1.0	0.3	17.3	4.6
	3600	6.4	7.5	1.0	0.3	16.3	4.8
	3800	3.8	6.3	1.0	0.3	15.4	4.2
	4350	4.8	6.5	0.9	0.3	14.2	3.6
	4800	5.8	6.8	0.9	0.3	14.1	3.5
	5500	6.0	6.8	0.9	0.3	14.0	3.5

Table S6: Calculated average pore sizes (diameter) of all pores and selected pore populations (micro-, meso- and macropores) in heated Ni_xCo_{1-x}-struvite (x= 0.5, 0.8); Heated $Ni_{0.2}Co_{0.8}$-struvite shows no significant mesoporosity and therefore cannot be fitted.

M-struvite system	Ni#	all pores		microporous population (0-2 nm)		meso- and macropopulation (2-300 nm)	
		μ (diameter) [nm]	σ [nm]	μ (diameter) [nm]	σ [nm]	μ (diameter) [nm]	σ [nm]
Ni 20% Co 80%	0.2	-	-	-	-	-	-
Ni 50% Co 50%	0.5	49.7	33.6	1.1	0.5	50.5	33.3
Ni 80% Co 20%	0.8	31.6	30.1	1.0	0.2	51.4	40.6

Table S7: XANES Ni-K (8333 eV) pre-peak integration results of heated Ni-struvite in a t-series from 0-150 min and from hydrothermally synthesized Ni-dittmarite; fitting with a Gaussian Model; Note the change at t = 40 min in the pre-peak area.

Ni-struvite isothermally heated at T = 90°C, fit function: Gaussian							
t	**Phase composition**	**chemical formula**	**R^2 value**	**Pre-peak Area A_{pp} (err)**	**FWHM**	**Center**	**Max. Height**
0	Ni-struvite	$NH_4NiPO_4{\cdot}6H_2O$	0.999	0.0250(1)	1.792	8333.8	0.0131
10	Ni-struvite	$NH_4NiPO_4{\cdot}6H_2O$	0.999	0.0257(1)	1.707	8334.0	0.0142
20	amorphous	$NH_4NiPO_4{\cdot}6H_2O$	0.998	0.0252(2)	1.703	8334.0	0.0139
40	amorphous	$\approx NH_4NiPO_4{\cdot}H_2O$	0.998	0.0293(1)	1.744	8333.9	0.0158
60	amorphous	$\approx NH_4NiPO_4{\cdot}H_2O$	0.994	0.0291(1)	1.735	8333.9	0.0157
90	amorphous	$\approx NH_4NiPO_4{\cdot}H_2O$	0.994	0.0294(1)	1.754	8333.9	0.0157
120	amorphous	$\approx NH_4NiPO_4{\cdot}H_2O$	0.996	0.0301(1)	1.762	8333.9	0.0161
150	amorphous	$\approx NH_4NiPO_4{\cdot}H_2O$	0.999	0.0298(1)	1.744	8333.9	0.0160
1d (hydrothermal)	Ni-dittmarite	$NH_4NiPO_4{\cdot}H_2O$	0.999	0.0296(2)	1.714	8333.9	0.0162

Table S8: XANES Ni-K (8333 eV) and Co-K (7709 eV) pre-peak integration results of selected Ni_xCo_{1-x}-struvite precursors and heated products at T = 90°C and t = 1 d by fitting with a Gaussian model.

Pre-peak area integration results				**Ni_xCo_{1-x}-mixtures**		**fit function: Gaussian**		
Sample	**Ni#**	**K-edge**	**χ^2**	**R^2 value**	**Area (err)**	**FWHM**	**Max. Height**	**Center**
$Ni_{0.2}Co_{0.8}$-struvite	0.2	Ni	3.77E-08	0.998	0.025(1)	1.79	0.013	8333.0
$Ni_{0.5}Co_{0.5}$-struvite	0.5	(8333 eV)	7.68E-08	0.991	0.025(1)	1.87	0.013	8332.9
$Ni_{0.8}Co_{0.2}$-struvite	0.8		1.47E-07	0.982	0.025(1)	1.86	0.012	8333.0
$Ni_{0.2}Co_{0.8}$-PO_4 (90°C)	0.2		2.68E-07	0.983	0.020(1)	1.79	0.010	8333.4
$Ni_{0.5}Co_{0.5}$-PO_4 (90°C)	0.5		8.57E-08	0.994	0.023(1)	1.78	0.012	8333.4
$Ni_{0.8}Co_{0.2}$-PO_4 (90°C)	0.8		1.17E-07	0.984	0.024(1)	1.85	0.012	8333.4
$Ni_{0.2}Co_{0.8}$-struvite	0.2	Co	6.41E-08	0.992	0.025(1)	2.21	0.010	7708.7
$Ni_{0.5}Co_{0.5}$-struvite	0.5	(7709 eV)	6.25E-08	0.994	0.030(1)	2.32	0.012	7708.6
$Ni_{0.8}Co_{0.2}$-struvite	0.8		7.82E-08	0.993	0.032(2)	2.67	0.011	7708.6
$Ni_{0.2}Co_{0.8}$-PO_4 (90°C)	0.2		1.03E-07	0.994	0.034(2)	2.08	0.015	7708.5
$Ni_{0.5}Co_{0.5}$-PO_4 (90°C)	0.5		6.25E-08	0.998	0.045(2)	1.67	0.026	7708.5
$Ni_{0.8}Co_{0.2}$-PO_4 (90°C)	0.8		6.61E-08	0.999	0.046(2)	1.64	0.026	7708.6

Table S9: Summarized Ni- and Co-K-prepeak area integration results and phase composition derived by XRD of the Ni_xCo_{1-x}-mixtures before and after heating at T = 90°C; M = Ni_xCo_{1-x}.

Sample	Ni#	Ni-K-App (err)	Co- K-App (err)	XRD phase composition	Chemical composition
$Ni_{0.2}Co_{0.8}$-struvite	0.2	0.025(1)	0.025(1)	M-struvite	$NH_4MPO_4•6H_2O$
$Ni_{0.5}Co_{0.5}$-struvite	0.5	0.025(1)	0.030(1)	M-struvite	$NH_4MPO_4•6H_2O$
$Ni_{0.8}Co_{0.2}$-struvite	0.8	0.025(1)	0.032(2)	M-struvite	$NH_4MPO_4•6H_2O$
$Ni_{0.2}Co_{0.8}$-PO_4 (90°C)	0.2	0.020(1)	0.034(2)	M-dittmarite	$NH_4MPO_4•H_2O$
$Ni_{0.5}Co_{0.5}$-PO_4 (90°C)	0.5	0.023(1)	0.045(2)	M-dittmarite + amorphous	$NH_4MPO_4•H_2O$ + amorphous
$Ni_{0.8}Co_{0.2}$-PO_4 (90°C)	0.8	0.024(1)	0.046(2)	amorphous	amorphous

Table S10: Fit results parameter for Ni-struvite R-factor= 0.005.

sample	scattering path	degeneracy	σ^2	R_{diff} [Å]	R_{diff}^2 [Å²]	R_{model} [Å]	R_{fit} [Å]
Ni-struvite	Ni1-O1	4	0.009	-0.001	1.00E-06	2.046	**2.044**
NH_4NiPO_4•$6H_2O$	Ni1-O2	2	0.009	-0.001	1.00E-06	2.089	**2.088**
mean R_{fit} (err) [Å]	Ni1-O3-H1	4	-0.001	-0.207	4.29E-02	2.560	2.353
2.059(6)	Ni1-H2	5	0.012	-0.217	4.70E-02	2.586	2.369
R-factor	Ni1-H3	2	0.012	-0.217	4.70E-02	2.627	2.410
0.005	Ni1-H4	2	0.012	-0.217	4.70E-02	2.668	2.451
S_O^2 Amplitude reduction factor (err)	Ni1-O1-O1	6	-0.001	-0.207	4.29E-02	3.465	3.258
1.3(1)	Ni1-O3-O2	16	-0.001	-0.207	4.29E-02	3.530	3.322
ΔE	Ni1-N1	1	0.005	-0.186	3.47E-02	4.022	3.836
3.1(6)	Ni1-N2	2	0.005	-0.186	3.47E-02	4.111	3.925
	Ni1-O4	4	0.006	0.242	5.85E-02	4.084	4.326
	Ni1-O5	2	0.006	0.242	5.85E-02	4.162	4.404
	Ni1-O6	2	0.006	0.242	5.85E-02	4.200	4.442
	Ni1-O7	3	0.006	0.242	5.85E-02	4.272	4.514
	Ni1-O8	2	0.006	0.242	5.85E-02	4.329	4.571

Table S11: Fit results parameter for Ni-struvite heated at 90°C for 10 min (time series), R-factor= 0.008.

sample	scattering path	degeneracy	σ^2	R_{diff} [Å]	R_{diff}^2 [Å²]	R_{model} [Å]	R_{fit} [Å]
T=90°C, t = 10 min	Ni1-O1	4	0.008	-0.002	2.25E-06	2.046	**2.044**
~NH_4NiPO_4•$6H_2O$	Ni1-O2	2	0.008	-0.002	2.25E-06	2.089	**2.088**
mean R_{fit} (err) [Å]	Ni1-H1	2	0.015	-0.200	3.98E-02	2.365	2.165
2.06(1)	Ni1-H2	5	0.015	-0.200	3.98E-02	2.586	2.386
R-factor	Ni1-O3-H1	4	0.010	-0.163	2.66E-02	2.560	2.397
0.008	Ni1-H3	2	0.015	-0.200	3.98E-02	2.627	2.428
S_O^2 Amplitude reduction factor (err)	Ni1-H4	2	0.015	-0.200	3.98E-02	2.668	2.468
1.2(1)	Ni1-O1-O1	6	0.010	-0.163	2.66E-02	3.465	3.302
ΔE	Ni1-O3-O2	16	0.010	-0.163	2.66E-02	3.530	3.366
-0.4(7)	Ni1-N1	1	0.010	-0.163	2.66E-02	4.022	3.859
	Ni1-N2	2	0.010	-0.163	2.66E-02	4.111	3.948
	Ni1-O4	4	0.006	0.326	1.06E-01	4.084	4.410
	Ni1-O5	2	0.006	0.326	1.06E-01	4.162	4.488
	Ni1-O6	2	0.006	0.326	1.06E-01	4.200	4.526
	Ni1-O7	3	0.006	0.326	1.06E-01	4.272	4.599
	Ni1-P1	2	0.006	0.326	1.06E-01	4.368	4.694

Table S12:Fit results parameter for Ni-struvite heated at 90°C for 20 min (time series), R-factor= 0.009.

sample	scattering path	degeneracy	σ^2	R_{diff} [Å]	R_{diff}^2 [Å^2]	R_{model} [Å]	R_{fit} [Å]
T=90°C, t = 20 min	Ni1-O1	5	0.008	-0.001	9.80E-07	2.046	**2.045**
~NH_4NiPO_4•$6H_2O$	Ni1-O2	1	0.008	-0.001	9.80E-07	2.089	**2.088**
mean R_{fit} (err) [Å]	Ni1-H1	5	0.019	-0.191	3.64E-02	2.586	2.395
2.053(6)	Ni1-H2	2	0.019	-0.191	3.64E-02	2.627	2.436
R-factor	Ni1-H3	2	0.019	-0.191	3.64E-02	2.668	2.477
0.009	Ni1-O1-O1	6	0.011	-0.198	3.94E-02	3.465	3.266
S_O^2 Amplitude reduction factor (err)	Ni1-O3-O2	16	0.011	-0.198	3.94E-02	3.530	3.331
1.2(1)	Ni1-N1	1	0.005	0.325	1.05E-01	4.022	4.347
ΔE	Ni1-O4	4	0.005	0.325	1.05E-01	4.084	4.409
-1.4(9)	Ni1-N2	2	0.005	0.325	1.05E-01	4.111	4.435
	Ni1-O5	2	0.005	0.325	1.05E-01	4.162	4.486
	Ni1-O6	2	0.005	0.325	1.05E-01	4.200	4.524
	Ni1-O7	3	0.005	0.325	1.05E-01	4.272	4.597
	Ni1-O8	2	0.005	0.325	1.05E-01	4.329	4.654
	Ni1-P1	2	0.005	0.325	1.05E-01	4.368	4.693

Table S13: Fit results parameter for Ni-struvite heated at 90°C for 40 min (time series), R-factor= 0.011.

sample	scattering path	degeneracy	σ^2	R_{diff} [Å]	R_{diff}^2 [Å²]	R_{model} [Å]	R_{fit} [Å]
T=90°C, t = 40 min	Ni1-O1	5	0.007	0.001	4.36E-07	2.043	**2.044**
~NH_4NiPO_4•H_2O	Ni1-O2	1	0.007	0.001	4.36E-07	2.108	**2.109**
mean R_{fit} (err) [Å]	Ni1-P1	1	0.029	-0.010	9.39E-05	2.734	2.724
2.097(6)	Ni1-O3	2	0.012	-0.217	4.69E-02	3.283	3.067
R-factor	Ni1-P2	3	0.029	-0.010	9.39E-05	3.187	3.177
0.011	Ni1-P3	1	0.029	-0.010	9.39E-05	3.274	3.264
S_O^2 Amplitude reduction factor (err)	Ni1-O4	2	0.012	-0.217	4.69E-02	3.546	3.329
0.95(6)	Ni1-Ni1	4	0.012	-0.217	4.69E-02	3.673	3.456
ΔE	Ni1-O5	2	0.012	-0.217	4.69E-02	3.767	3.550
-2.1(6)	Ni1-O6	2	0.012	-0.217	4.69E-02	3.800	3.583
	Ni1-O7	1	0.012	-0.217	4.69E-02	3.878	3.662
	Ni1-O8-P2	4	0.001	0.289	8.33E-02	3.399	3.687
	Ni1-O1-P3	2	0.001	0.289	8.33E-02	3.406	3.695
	Ni1-H1-O4	4	0.001	0.289	8.33E-02	3.628	3.917
	Ni1-O8-Ni1	8	0.001	0.289	8.33E-02	3.935	4.223
	Ni1-H2-O5	4	0.001	0.289	8.33E-02	3.969	4.257
	Ni1-P1-O9	2	0.001	0.289	8.33E-02	4.022	4.310
	Ni1-P1-O7	2	0.001	0.289	8.33E-02	4.058	4.347
	Ni1-O10	2	0.006	0.284	8.05E-02	4.111	4.395
	Ni1-O11	2	0.006	0.284	8.05E-02	4.160	4.444
	Ni1-O1-O6	4	0.001	0.289	8.33E-02	4.191	4.480
	Ni1-O12	2	0.006	0.284	8.05E-02	4.224	4.508
	Ni1-O13	2	0.006	0.284	8.05E-02	4.733	5.017
	Ni1-O8-O13	4	0.001	0.289	8.33E-02	4.831	5.119

Table S14: Fit results parameter for Ni-struvite heated at 90°C for 60 min, R-factor= 0.013.

sample	scattering path	degeneracy	σ^2	R_{diff} [Å]	R_{diff}^2 [Å²]	R_{model} [Å]	R_{fit} [Å]
T=90°C, t = 60 min	Ni1-O1	5	0.007	0.005	2.84E-05	2.043	**2.049**
~NH_4NiPO_4•H_2O	Ni1-O2	1	0.007	0.005	2.84E-05	2.108	**2.113**
mean R_{fit} (err) [Å]	Ni1-P1	2	0.005	0.025	6.20E-04	3.187	3.212
2.10(3)	Ni1-P2	1	0.005	0.025	6.20E-04	3.274	3.299
R-factor	Ni1-N1	1	0.003	-0.065	4.25E-03	4.022	3.957
0.013	Ni1-N2	2	0.003	-0.065	4.25E-03	4.111	4.046
S_O^2 Amplitude reduction factor (err)	Ni1-O3	4	0.005	0.162	2.62E-02	4.084	4.246
0.95(6)	Ni1-O4-O5	4	-0.008	-0.220	4.83E-02	4.488	4.268
ΔE	Ni1-O6	2	0.005	0.162	2.62E-02	4.162	4.324
-1.4(6)	Ni1-O7	2	0.005	0.162	2.62E-02	4.200	4.362
	Ni1-P1	2	0.005	0.025	6.20E-04	4.368	4.393
	Ni1-O8	3	0.005	0.162	2.62E-02	4.272	4.434
	Ni1-O9	2	0.005	0.162	2.62E-02	4.329	4.491

Table S15: Fit results parameter for Ni-struvite heated at 90°C for 90 min, R-factor= 0.008.

sample	scattering path	degeneracy	σ^2	R_{diff} [Å]	R_{diff}^2 [Å²]	R_{model} [Å]	R_{fit} [Å]
T=90°C, t = 90 min	Ni1-O1	5	0.008	-0.001	2.13E-06	2.043	**2.042**
~NH_4NiPO_4•H_2O	Ni1-O2	1	0.008	-0.001	2.13E-06	2.108	**2.107**
mean R_{fit} (err) [Å]	Ni1-P1	1	0.018	0.073	5.26E-03	2.734	2.806
2.053(6)	Ni1-P2	3	0.018	0.073	5.26E-03	3.187	3.259
R-factor	Ni1-O3	4	0.031	-0.466	2.17E-01	3.767	3.301
0.008	Ni1-O4	8	0.031	-0.466	2.17E-01	3.800	3.334
S_O^2 Amplitude reduction factor (err)	Ni1-P3	1	0.018	0.073	5.26E-03	3.274	3.346
1.07(7)	Ni1-O5	2	0.001	0.080	6.45E-03	3.283	3.363
ΔE	Ni1-O6	8	0.031	-0.466	2.17E-01	3.878	3.413
-3.0(6)	Ni1-Ni2	4	0.013	-0.161	2.58E-02	3.673	3.512
	Ni1-O7	2	0.001	0.080	6.45E-03	3.546	3.626
	Ni1-O8	4	0.031	-0.466	2.17E-01	4.111	3.646
	Ni1-O9	8	0.031	-0.466	2.17E-01	4.160	3.695
	Ni1-O10	10	0.031	-0.466	2.17E-01	4.224	3.759

Table S16: Fit results parameter for Ni-struvite heated at 90°C for 120 min, R-factor= 0.010.

sample	scattering path	degeneracy	σ^2	R_{diff} [Å]	R_{diff}^2 [Å²]	R_{model} [Å]	R_{fit} [Å]
T=90°C, t = 120 min	Ni1-O1	5	0.008	-0.005	2.59E-05	2.043	**2.038**
~NH_4NiPO_4•H_2O	Ni1-O2	1	0.008	-0.005	2.59E-05	2.108	**2.103**
mean R_{fit} (err) [Å]	Ni1-P1	1	0.023	0.117	1.36E-02	2.734	2.850
2.04(4)	Ni1-O3	2	0.014	-0.087	7.57E-03	3.283	3.196
R-factor	Ni1-P2	3	0.023	0.117	1.36E-02	3.187	3.303
0.007	Ni1-O4	2	0.007	-0.416	1.73E-01	3.767	3.351
S_O^2 Amplitude reduction factor (err)	Ni1-P3	4	0.007	-0.416	1.73E-01	3.800	3.384
1.0(1)	Ni1-O5	1	0.023	0.117	1.36E-02	3.274	3.390
ΔE	Ni1-O6	4	0.014	-0.087	7.57E-03	3.546	3.459
-3.2(9)	Ni1-Ni2	4	0.007	-0.416	1.73E-01	3.878	3.463
	Ni1-O7	4	0.014	-0.087	7.57E-03	3.673	3.586
	Ni1-O8	4	0.007	-0.416	1.73E-01	4.111	3.695
	Ni1-O9	4	0.007	-0.416	1.73E-01	4.160	3.744
	Ni1-O10	2	0.007	-0.416	1.73E-01	4.224	3.809

Table S17: Fit results parameter for Ni-struvite heated at 90°C for 150 min, R-factor= 0.009.

sample	scattering path	degeneracy	σ^2	R_{diff} [Å]	R_{diff}^2 [Å²]	R_{model} [Å]	R_{fit} [Å]
T=90°C, t = 150 min	Ni1-O1	5.000	7.04E-03	4.10E-04	1.68E-07	2.043	**2.044**
~$NH_4NiPO_4•H_2O$	Ni1-O2	1.000	7.04E-03	4.10E-04	1.68E-07	2.108	**2.109**
mean R_{fit} (err) [Å]	Ni1-P1	1.000	2.41E-02	4.39E-02	1.93E-03	2.734	2.778
2.054(2)	Ni1-P2	3.000	2.41E-02	4.39E-02	1.93E-03	3.187	3.231
R-factor	Ni1-P3	1.000	2.41E-02	4.39E-02	1.93E-03	3.274	3.318
0.009	Ni1-O3	2.000	1.37E-03	8.92E-02	7.95E-03	3.283	3.372
S_O^2 Amplitude reduction factor (err)	Ni1-Ni2	4.000	1.26E-02	-1.64E-01	2.68E-02	3.673	3.509
0.97(6)	Ni1-O4	2.000	1.37E-03	8.92E-02	7.95E-03	3.546	3.635
ΔE	Ni1-O5	2.000	2.16E-02	3.09E-01	9.57E-02	3.767	4.076
-2.1(6)	Ni1-O6	2.000	2.16E-02	3.09E-01	9.57E-02	3.800	4.109
	Ni1-O7	1.000	2.16E-02	3.09E-01	9.57E-02	3.878	4.188
	Ni1-O8	8.000	2.16E-02	3.09E-01	9.57E-02	4.111	4.420
	Ni1-O9	4.000	2.16E-02	3.09E-01	9.57E-02	4.160	4.469
	Ni1-O10	4.000	2.16E-02	3.09E-01	9.57E-02	4.224	4.534

Table S18: Fit results parameter for Ni-monohydrate synthesized in a hydrothermal route, R-factor= 0.012.

sample	scattering path	degeneracy	σ^2	R_{diff} [Å]	R_{diff}^2 [Å²]	R_{model} [Å]	R_{fit} [Å]
Ni-monohydrate	Ni1-O1	3	0.006	-2.60E-02	6.75E-04	2.043	**2.017**
$NH_4NiPO_4•H_2O$	Ni1-O2	1	0.006	-2.60E-02	6.75E-04	2.108	**2.082**
mean R_{fit} (err) [Å]	Ni1-O3	2	0.006	-2.60E-02	6.75E-04	2.149	2.123
2.063(9)	Ni1-P1	1	0.009	1.67E-02	2.78E-04	2.734	2.751
R-factor	Ni1-O4	2	0.027	-2.34E-01	5.47E-02	3.283	3.049
0.012	Ni1-P2	3	0.009	1.67E-02	2.78E-04	3.187	3.203
S_O^2 Amplitude reduction factor (err)	Ni1-P3	1	0.009	1.67E-02	2.78E-04	3.274	3.291
0.99(7)	Ni1-O5	8	0.027	-2.34E-01	5.47E-02	3.546	3.312
ΔE	Ni1-O6	2	0.027	-2.34E-01	5.47E-02	3.767	3.533
-1.3(6)	Ni1-O7	8	0.027	-2.34E-01	5.47E-02	3.878	3.645
	Ni1-Ni2	4	0.011	3.34E-01	1.12E-01	3.673	4.007
	Ni1-O8	4	0.011	3.34E-01	1.12E-01	3.800	4.134
	Ni1-O9	4	0.011	3.34E-01	1.12E-01	4.111	4.445
	Ni1-O10	4	0.011	3.34E-01	1.12E-01	4.160	4.494
	Ni1-O11	4	0.011	3.34E-01	1.12E-01	4.224	4.558

References SI

1. J. Hövelmann, T. M. Stawski, R. Besselink, H. M. Freeman, K. M. Dietmann, S. Mayanna, B. R. Pauw and L. G. Benning, *Nanoscale*, 2019, **11**, 6939-6951.
2. A. G. Baldwin, Y. Yang, N. J. Bridges and J. C. Braley, *J Phys Chem B*, 2016, **120**, 12184-12192.
3. O. Lehmann, H. Meyssamy, K. Kömpe, H. Schnablegger and M. Haase, *J. Phys. Chem. B.*, 2003, **107**, 7449-7453.
4. S. Visser and S. Cooper, *Macromolecules*, 1991, **24**, 2584-2593.
5. D. J. Kinning and E. L. Thomas, *Macromolecules*, 1984, **17**, 1712-1718.